DOI: https://doi.org/10.2138/am-2022-8412. http://www.minsocam.org/

Revision 1

Word Count: 10649

Discrete Late Jurassic Sn Mineralizing Events in the Xianghualing Ore District, South China: Constraints from Cassiterite and Garnet U-Pb Geochronology

Kexin Wang[1], Degao Zhai[1*], Anthony E. Williams-Jones[2], Dengfeng Li[3], Jiajun Liu[1]

[1]State Key Laboratory of Geological Processes and Mineral Resources, and School of Earth Sciences and Resources, China University of Geosciences, Beijing 100083, China

[2]Department of Earth and Planetary Sciences, McGill University, Quebec, H3A 0E8, Canada

[3]School of Marine Sciences, Sun Yat-sen University, Guangzhou 510006, China

[*]E-mail: dgzhai@cugb.edu.cn

Revised submission to: *American Mineralogist*

With 43 pages, 13 Figures and 2 Tables

24-May-2022

ABSTRACT

Numerous skarn-type Sn deposits have been identified in the Nanling Range (South China), of which the Shizhuyuan W-Sn-Bi-Mo, Xianghualing Sn, Jinchuantang Sn-Bi, and Hehuaping Sn deposits are the largest. The Xianghualing deposit, which is the focus of this study, hosts a resource of 0.17 Mt Sn grading 0.93-1.39 wt% SnO_2. Whether the distal skarn-type mineralization and the cassiterite-sulfide vein-type orebody in the Xianghualing district are genetically related to the Laiziling granitic pluton, which produced the proximal skarn-type Sn mineralization, however, is still unknown. The Xianghualing Sn mineralization occurs exclusively as cassiterite and has been subdivided into four ore-types: (1) lenticular proximal skarn ore (Cst I) containing the mineral assemblage cassiterite-pyrrhotite-chalcopyrite-actinolite-wollastonite; (2) layered distal skarn ore (Cst II) containing the mineral assemblage cassiterite-pyrrhotite-chalcopyrite-actinolite; (3) vein cassiterite-sulfide ore (Cst III) distal from the skarn and associated granite containing the mineral assemblage cassiterite-arsenopyrite-pyrrhotite-muscovite-fluorite; and (4) veinlet Sn-Pb-Zn ore (Cst IV) distal from the skarn and associated granite containing the mineral assemblage cassiterite-galena-sphalerite-topaz-quartz. Here, we report the results of in situ laser ablation inductively coupled plasma mass spectrometric (LA-ICP-MS) U-Pb age determinations for garnet from the Xianghualing skarn and the above four types of cassiterite. Our age determinations indicate that there were two independent magmatic-hydrothermal events at ~160 and 156~150 Ma, both of which led to Sn mineralization. The first Sn mineralization event at ~160 Ma (Cst IV U-Pb ages of

159.6 ± 1.4 to 158.5 ± 0.8 Ma) is interpreted to have been associated with a speculative unexposed granitic pluton, which is coeval with the nearby Jianfengling granite intrusion. The second Sn mineralization event at 156~150 Ma (Cst I to Cst III U-Pb ages of 155.9 ± 0.7 to 152.3 ± 1.1 Ma and garnet U-Pb ages of 153.6 ± 7.6 to 151.5 ± 3.5 Ma) is genetically related to the adjacent Laiziling granitic intrusion (152.8 ± 1.2 Ma, zircon U-Pb age). This event was responsible for the bulk of the Sn resource (>95%). Our age determinations provide convincing evidence for superimposed Jurassic Sn mineralizing systems at Xianghualing. They also show the value of combining garnet and cassiterite U-Pb age determinations in order to constrain the timing of skarn and Sn mineralization and distinguish discrete Sn mineralizing events in a protracted metallogenic history.

Keywords: Cassiterite U-Pb dating; Garnet U-Pb dating; Xianghualing Sn deposit; Late Jurassic; South China

INTRODUCTION

Metal zonation at the deposit and ore district scale is a characteristic of skarn-dominated metallogenic provinces and is the result of processes ranging from those that lead to the development of skarn orebodies proximal to the causative granite to those forming distal skarns and hydrothermal vein-type orebodies (Newberry et al., 1991; Meinert, 2005; Williams-Jones et al., 2010; Mao et al., 2013; Chang et al., 2019). This zonation provides a potentially important tool for use in the exploration for skarn-hosted mineral deposits (Meinert et al., 1997; Wu S et al., 2018). However, because the distal skarn and vein-type orebodies commonly lack an obvious spatial association with granitic plutons and their distribution is controlled mostly by stratigraphy and faults, the genetic relationships between these orebodies and the causative plutons are difficult to determine (Newberry et al., 1991; Baker et al., 2004; Wu S et al., 2018). This difficulty is compounded by the fact that the ages of distal skarns and their associated mineralization are rarely known to the required degree of accuracy (Chiaradia et al., 2009, 2013; Zhai et al., 2014, 2019; Zhao et al., 2021).

Skarns are among the most common hosts for economic mineralization in China and contribute ~87% of the Sn resources of the country (~8.9 Mt) (Chang et al., 2019). About 60% of these resources are located in the Nanling Range, South China (Chen et al., 2013). The Shizhuyuan and the Xianghualing are the two largest skarn tin deposits in the Nanling Range, and are considered to be genetically related to proximal Mesozoic granites (Yuan et al., 2007, 2008, 2019; Mao et al., 2011; Wu S et al., 2018; Zhao et al., 2018). Significantly, in the context of the zonation referred to above, recent exploration has identified a series of Sn-Pb-Zn-Ag veins that are distal to these Sn skarns and their associated granitic plutons (Zhong et al., 2014; Wu S et al., 2018; Zhao et al., 2018; Chang et al., 2019). In the case of the Shizhuyuan district, Wu S et al. (2018) and Zhao et al. (2018) used geochronological, fluid inclusion, and stable isotope data to conclude that there is a genetic relationship between the distal Pb-Zn-Ag veins and the skarn W-Sn-Mo-Bi mineralization that is proximal to its genetically-related granitic pluton. The possible relationship between the distal Sn-Pb-Zn veins and the skarn type Sn mineralization in the Xianghualing district, however, has not been investigated. This can be achieved through a combination of careful field investigation and precise radiometric age determinations aimed at determining the timing of ore mineral precipitation (Mathur et al., 2005; Chiaradia et al., 2009, 2013; Sillitoe, 2010; Zhai et al., 2017; Zhao et al., 2018).

In situ LA-ICP-MS dating of skarn minerals, such as garnet, can constrain the age of skarn formation directly (Deng et al., 2017; Li D et al., 2018, 2019; Marfin et al., 2020; Hong et al., 2021, 2022). This is because garnet may contain significant concentrations of U and has a high closure temperature (> 800°C; Mezger et al., 1989), especially the grossular-andradite series ($Ca_3Al_2Si_3O_{12}$-$Ca_3Fe_2Si_3O_{12}$) (DeWolf et al., 1996; Yudintsev et al., 2002). In the case of tin skarns, the mineralization can be dated directly because much of the tin occurs as cassiterite, which can incorporate significant U and has a high closure temperature (for a 1 μm diameter crystal this temperature can reach 560°C and for a 1mm diameter crystal it can reach 860°C, Zhang et al., 2011). Consequently, a number of studies have used garnet and cassiterite to investigate the geochronology of skarn-related Sn mineralization, including several applied to the deposits of the Nanling Range (Zhang et al., 2015; Li et al., 2019; Xiong et al., 2020).

In this contribution, we report the results of a detailed geochronological study using in situ LA-ICP-MS U-Pb radiometric methods applied to cassiterite and garnet in the Xianghualing skarn, cassiterite in Sn-Pb-Zn veinlets distal to the skarn, and zircon in the granite proximal to the skarn. These results show that the Xianghualing Sn mineralization was the product of two temporally separate late Jurassic mineralizing events, which has helped us to develop a new genetic model for Sn mineralization in the Xianghualing district.

REGIONAL GEOLOGY SETTING

The Nanling Range (longitude 110°E-116°E, latitude 24°N-27°N) is located in the central part of the South China Block, which is composed of the Yangtze Block and the Cathaysia Block (Fig. 1A; Chen and Jahn, 1998; Li et al., 2002, 2008; Chen et al., 2013; Wang et al., 2013). The regional stratigraphy comprises a basement of Sinian to Ordovician clastic sedimentary rocks, which were overlain by Devonian to Triassic limestone, marlstone, and clastic sedimentary rocks, and, in turn, by Jurassic to Cretaceous clastic sedimentary rocks, volcanic rocks and red beds (Chen et al., 2013). The tectonic framework for the region is provided by three fault systems, which are mainly NE-, NNE-, and EW-trending. Among them, the dominant system is the NE-trending Chaling-Linwu system, which controlled the spatial distribution of granitic intrusions and their associated W-Sn deposits (Zhou and Li, 2000; Zhou et al., 2006; Hu and Zhou, 2012; Yuan et al., 2019). Mesozoic granitic intrusions are common in the region, especially Jurassic biotite and two-mica granites (Fig. 1B; Chen et al., 2013; Zhao et al., 2018; Yuan et al., 2019). The Sn-W mineralization is mainly related to the Jurassic granitic plutons, e.g., the Qianlishan, Qitianling, Huangshaping and Laiziling plutons, which are highly-evolved, Li- and F-bearing A-type granites (Shu et al., 2011; Sun et al., 2012; Li H et al., 2018; Xiao et al., 2019). Ore deposits in the region include Sn and W-Sn skarns (e.g., Shizhuyuan W-Sn-Mo-Bi, Wu S et al., 2018, Xianghualing Sn-Pb-Zn, Yuan et al., 2008), Sn and W-Sn greisens (e.g., Da'ao Sn-W, Fu et al., 2007; Tiantangshan Sn, Jia et al., 2018), W-Sn quartz veins (e.g., Maoping W-Sn, Chen et al., 2019, Piaotang W-Sn, Zhang et al., 2017b), and porphyry Sn deposits (e.g., Jiepailing Sn-Be-F, Yuan et al., 2015; Yanbei Sn, Li Q et al., 2018). The tin mineralization is restricted to the western part of the region, where it occurs mainly in skarns hosted by carbonate rocks and to a much lesser extent in cassiterite-sulfide veins hosted by siliciclastic rocks (Yuan et al., 2019). Tin and tungsten deposits in the Nanling region vary in age from Silurian to Cretaceous, but most were emplaced in the late Jurassic (i.e., between 160 and 150 Ma; Hua et al., 2005; Mao et al., 2013).

GEOLOGY OF THE XIANGHUALING DEPOSIT

The Xianghualing ore district is located on the northern margin of the central part of the Nanling Range (Fig. 1C), which coincides with the intersection of the NE-trending Chenzhou-Linwu fault zone and a NS-trending fault zone. A conspicuous feature of the district is a tectono-magmatic dome that is composed mainly of Paleozoic rocks. The core of the dome is a Cambrian metamorphic rock series composed of sandstone and slate that were metamorphosed to greenschist facies. The flanks of the dome are composed of conglomerate, sandstone, siltstone and shale of the middle Devonian Tiaomajian formation (D_2t), limestone and dolomitic limestone of the Qiziqiao formation (D_2q), dolomitic limestone and sandstone of the upper Devonian Shetianqiao formation (D_3s), and Carboniferous carbonate rocks, all of which form a sedimentary package that is separated from the underlying basement by an angular unconformity (Figs. 1C and 2). The strata hosting the ores are mainly Devonian limestone and sandstone and Cambrian sandstone (Yuan et al., 2008; Jiang et al., 2018; Xie et al., 2018). The main ore-controlling faults are a group of tensional-shear conjugate normal faults, i.e., the NE-trending Xijianchong fault (F1) and Nanfengjiao fault (F101), the NW-trending Tieshaping fault (F2) and the Zimushan fault (F3) (Fig. 1C). The igneous rocks exposed in the general vicinity of the Xianghualing deposit are the Laiziling, Jianfengling, Tongtianmiao and Yaoshanli granites, which are of Jurassic age (Fig. 1C). A number of Sn-Pb-Zn ore deposits occur in or adjacent the Laiziling and Jianfengling granites (Fig. 1C).

The Xianghualing tin deposit has a close spatial, temporal and genetic relationship with the Laiziling biotite granite (Fig. 2; Yuan et al., 2007; Wu J et al., 2018). This granite is characterized by multiple intrusions and has been subdivided into four vertical zones (from bottom to top), i.e., a biotite granite zone, an albite granite zone, a greisen zone, and a pegmatite zone (Fig. 3A). The alteration and tin mineralization are zonally distributed from the pluton to the surrounding rocks, i.e., the dominant alteration assemblages are garnet-diopside-actinolite-vesuvianite, chlorite-carbonate and marble, and the corresponding metal associations are Sn (W), Sn-Pb-Zn, and Pb-Zn (Fig. 3B). Two skarn-types are observed in the Xianghualing tin district. The first is a proximal skarn, which occurs as layers, lenses and veins in the contact zone between granite and the Devonian wall rock, i.e., sandstone of the Tiaomajian formation (D_2t) and carbonate of the Qiziqiao formation (D_2q) (Fig. 2, 3B,4A, 5A).

The principal skarn minerals are garnet, diopside, vesuvianite, tremolite, and actinolite (Fig 5B, C). The second type is the distal skarn, which is layer-like and occurs along the unconformity between sandstone of the Cambrian (Є) and sandstone of the Tiaomajian formation (D_2t) (Fig. 4B, 5F); the main skarn mineral is actinolite (Fig. 5F).

The Xianghualing tin deposit is composed of three ore blocks that are distributed along and straddle the NE-trending Xijianchong fault (F1) (Fig. 2A), namely, the Xinfeng, Taiping and Tangguanpu ore blocks. Based on field observations, crosscutting relations and mineral assemblages, the Xianghualing mineralization has been subdivided into four stages (Fig. 6), namely prograde skarn (I), retrograde skarn (II), quartz-cassiterite-sulfide (III) and carbonate (IV) stages. In contrast to many other skarn-type deposits (Mei et al., 2014; Zhai et al., 2014), the oxide stage is poorly developed at Xianghualing, and only a small proportion of magnetite is present. Stage II and Stage III are the main Sn mineralization stages. Four types of Sn mineralization have been recognized: proximal skarns, distal skarns, cassiterite-sulfide veins, and distal Sn-Pb-Zn veinlets. Proximal skarn orebodies occur as lenticular structures varying in length from 100 to 3000 m and in thicknesses from 0.9 to18.9 m (Fig. 3B, 4A, 5A, B). Their Sn grades vary between 0.02 and 3.97 wt% (Zhong et al., 2014) and the associated mineral assemblage is actinolite-biotite-cassiterite-pyrrhotite-chalcopyrite (Fig. 5C). The distal skarn orebodies are layered (Fig. 4B, 5F), vary in length from 1400 to 1700 m and range in thicknesses from 0.35 to 4.08 m. Their Sn grades are between 0.1 and 4.6 wt% (Zhong et al., 2014) and represent a rock

DOI: https://doi.org/10.2138/am-2022-8412. http://www.minsocam.org/

containing the mineral assemblage actinolite-tremolite-phlogopite-biotite-quartz-cassiterite-pyrite-pyrrhotite-chalcopyrite (Fig. 5F). The cassiterite-sulfide vein orebodies comprise the minerals cassiterite, arsenopyrite and pyrrhotite and are both parallel to and cross-cut bedding structures, and are controlled by faults, such as F1 (Fig. 4A). They vary in length from 1100 to 2100 m and in thicknesses from 0.4 to 14.1 m. Their Sn grades vary between 0.12 and 10.29 wt% (Zhong et al., 2014) and, in addition to cassiterite and the sulfides mentioned above, they contain quartz, muscovite and fluorite (Fig. 5G, H). The distal Sn-Pb-Zn veinlet orebodies comprise swarms of quartz veinlets (0.5 to 1.5 cm thick; Fig. 4C, 5I, J) that are located in the hanging wall of the F1 fault in the Tangguanpu ore block, which is hosted by sandstones of the Tiaomajian formation (D_2t) (Fig. 4C, 5I, J). The distal Sn-Pb-Zn veinlets are about 3 km horizontally from the Laiziling pluton (Fig. 2) and 100 m vertically below the surface (Fig 4C), and there is no exposed proximal intrusion. In addition to quartz, they contain cassiterite, topaz, galena, sphalerite and pyrite (Fig. 4C, 5I-K) and their integrated Sn grade ranges from 0.50 to 1.54 wt%.

SAMPLES AND ANALYTICAL METHODS

Samples for detailed geochronological study were collected from drill core and underground workings in the Xianghualing deposit. Garnet and cassiterite-sulfide samples were collected in the Xinfeng ore block and the proximal, distal skarn ores and distal Sn-Pb-Zn veinlet ores were collected in the Tangguanpu ore block.

Zircon LA-ICP-MS U-Pb dating

Zircon crystals used for LA-ICP-MS U-Pb dating were separated from biotite granite in the Laiziling pluton (sample No. 19XHL-12), which was sampled on the 580 m level tunnel in the Tangguanpu ore block (Fig. 5A, D, E). The separation was conducted at the Langfang Tuoxuan Rock and Mineral Testing Service Co., Ltd., China. Zircon crystals were separated by standard heavy-liquid and magnetic techniques and further purified by handpicking under a binocular microscope. After separation, the zircon crystals were examined in transmitted light and reflected light using an optical microscope to determine the crystal morphology and cathodoluminescence (CL) images were prepared to observe the internal structure of the crystals. The CL images were acquired using a JEOL JXA-8900RL scanning electron microscope (SEM) at the Beijing GeoAnaly Technology Co. Ltd., China.

The zircon U-Pb dating was carried out using LA-ICP-MS in the State Key Laboratory of Geological Processes and Mineral Resources at the China University of Geosciences, Beijing (CUGB). The crystals were ablated using an excimer laser ablation system (New-Wave 193ss). An Agilent 7500a four-stage ICP-MS instrument was used for the analyses. A laser spot size of 25 μm, a laser energy density of 8.5 J/cm^2, and a repetition rate of 10 Hz were employed during the analysis. Helium and argon were used as carrier and makeup gases, respectively, and were mixed via a T-connector before entering the ICP. Each analysis involved a 20 s gas blank and 45 s signal acquisition. Uranium, Th, and Pb concentrations were calibrated using ^{29}Si as an internal standard and NIST 610 glass as the reference standard. Zircon 91500 was used as the external standard and was employed to correct for instrumental mass bias and depth-dependent elemental and isotopic fractionation (Wiedenbeck et al., 1995). The zircon standard, Qinghu, was used as a secondary standard to monitor any deviation in the age measurement/calculation. The mean $^{206}Pb/^{238}U$ age obtained for Qinghu is 160.8 ± 1.6 Ma (MSWD = 0.25, n = 6), which is consistent with the recommended age (159.5 ± 0.2 Ma; Li et al., 2013). The raw data reduction was performed off-line using GLITTER 4.4.4 software developed by Macquarie University. Age calculations were conducted and concordia plots prepared using Isoplot 3.0 (Ludwig, 2003). The uncertainty in the age determinations corresponds to the 95 % confidence level and error ellipses represent the 1 sigma deviation.

Garnet LA-ICP-MS U-Pb dating

Uranium-lead age determinations were conducted on two garnet-bearing samples of prograde skarn collected from the 0 m level tunnel in the Xinfeng ore block (19XHL-18 and 19XHL-45-1). Backscattered electron (BSE) images of the garnet were acquired using a TESCAN MIRA3 electron microprobe at the Guangzhou Tuoyan Testing Technology Co., Ltd., China prior to LA-ICP-MS analysis.

The compositions of the minerals were determined using a JEOL EPMA-1720H Superprobe at the electron microprobe laboratory, Zhejiang University, China. The operating conditions were a 15 kV accelerating voltage, 20 nA beam current, 1-2 μm beam diameter, 10 s counting time and the ZAF correction procedure for data reduction. For further detail on the analytical procedure, readers are referred to Yu et al. (2018).

The garnet LA-ICP-MS U-Pb dating was carried out at the Key Laboratory of Marine Resources and Coastal Engineering, Sun Yat-sen University, China. The analyses were performed using a 193 nm ArF excimer laser ablation system (GeoLasPro) coupled with an Agilent 7700x ICP-MS. A spot size of 60 µm was used with an energy density of 5 J/cm^2 and a repetition rate of 5 Hz. Helium and argon were used as carrier and makeup gases, respectively, and were mixed via a T-connector before entering the ICP. Each spot analysis incorporated a background acquisition of approximately 20 s followed by 45 s of sample data acquisition. The glass, NIST SRM 610 (Pearce et al., 1997), was used as the external standard to calibrate the trace element analysis of the garnet, and ^{29}Si was used as an internal standard. Zircon 91500 (Wiedenbeck et al., 1995) was used as the external standard for the U-Pb dating as the matrix effect has been shown to be minor for garnet U-Pb dating (Deng et al., 2017). Garnet standards WS-20 and GRT-1 were used to monitor the garnet age determinations. They yielded Tera-Wasserburg concordia intercept ages of 1152.2 ± 5.8 and 137.0 ± 2.3 Ma, respectively, which are the same as the published ages within the analytical uncertainty (Li et al., 2022; Zhang et al., 2019). The raw data reduction was performed off-line using Iolite 4.0 software (Petrus and Kamber, 2012). The analytical results for GRT-1 and WS-20 are presented in Appendix Table 3. The program IsoplotR online toolbox (Vermeesch, 2018) was used to calculate the U-Pb ages and draw Tera-Wasserburg concordia diagrams. The errors in the ages represent the 95 % confidence level and the error ellipses represent a 2 sigma deviation.

Cassiterite LA-ICP-MS U-Pb dating

Cassiterite samples for LA-ICP-MS U-Pb dating were collected from the proximal skarn-type orebody (sample 19XHL-10-6 on the 580 m level in the Tangguanpu ore block), the distal skarn-type orebody (sample 19XHL-3 on the 654 m level in the Tangguanpu ore block), the cassiterite-sulfide vein-type orebody (sample 19XHL-17-1 and 19XHL-24 on the 0 m level in the Xinfeng ore block), and the distal Sn-Pb-Zn veinlet-type orebody (sample ZK7003-11 from drill core ZK7003 in the Tangguanpu ore block). Cathodoluminescence (CL) images were obtained for the cassiterite crystals prior to LA-ICP-MS analysis. The CL images were taken at the Guangzhou Tuoyan Testing Technology Co., Ltd., China using a Zeiss Supra 55 field emission SEM equipped with a MonoCL4 luminoscope.

The cassiterite U-Pb ages (samples of 19XHL-10-6, 19XHL-17-1, 19XHL-24 and ZK7003-11) were determined at the Guangzhou Tuoyan Testing Technology Co., Ltd., China, using an iCAP RQ ICP-MA coupled to a 193 nm ArF Excimer laser ablation system (NWR193). A laser spot size of 50 μm, a laser energy density of 5 J/cm^2, and a repetition rate of 8 Hz were employed during the analyses. Helium and argon were used as carrier and makeup gases, respectively, and were mixed via a T-connector before entering the ICP. Each spot analysis involved a background acquisition of approximate 20 s followed by 40 s of sample data acquisition. The NIST SRM610 standard and an in-house cassiterite standard, AY-4, were used for external elemental and isotopic calibration, respectively. The AY-4 standard was collected from the Anyuan skarn-type tin deposit of the Furong tin ore field in the middle Nanling Range. This cassiterite sample was analyzed by Yuan et al. (2011) using ID-TIMS and returned an U-Pb age of 158.2 ± 0.4 Ma. Raw data reduction was performed off-line using Isoplot 4.0 software (Petrus and Kamber, 2012). The IsoplotR online toolbox (Vermeesch, 2018) was used to calculate the U-Pb ages and draw Tera-Wasserburg concordia diagrams. The uncertainties in the ages correspond to the 95% confidence level and the error ellipses represent 2 sigma deviations. The cassiterite U-Pb age of sample 19XHL-3 was determined at Yanduzhongshi Geological Analysis Laboratories Ltd., China, using an Analytikjena M90 quadrupole ICP-MS equipped with a 193 nm NWR193 ArF excimer laser. A laser spot size of 42 μm, a laser energy density of 4 J/cm^2, and a repetition rate of 8 Hz were employed during the analysis. Each cassiterite analysis began with a 20 s blank gas measurement followed by 40 s of analysis with the laser switched on. The downhole fractionation, instrument drift and mass bias correction factors for the Pb/U ratios of the cassiterite were calculated from two analyses of the primary AY-4 standard (Yuan et al., 2011), and analyses of secondary standards, i.e., the Cligga Head (Tapster and Bright, 2020) and Emmaville cassiterites (Prichard, 2013). These analyses were conducted at the beginning of each session and after 10 analyses of the cassiterite samples. The data reduction was based on the method outlined in Meffre et al. (2008). The uncertainties in the ages represent the 95 % confidence and the error ellipses correspond to the 1 sigma deviation.

RESULTS

Zircon LA-ICP-MS U-Pb dating

The zircon crystals of the biotite granite in the Laiziling pluton (sample No. 19XHL-12), for which U-Pb radiometric ages were determined, are euhedral and prismatic (Fig. 9), with obvious oscillatory zoning and no inherited cores, which is consistent with their magmatic origin (Davis et al., 2003; Hoskin and Schaltegger, 2003). The crystal length ranges from 60 to 120 μm and the length-to-width ratio varies from 1:1 to 3.5:1. Thorium and U concentrations vary considerably, from 222 to 3056 ppm (1230 ppm on average) and 422 to 9846 ppm (3652 ppm on average), respectively. The Th/U ratios range from 0.27 to 0.78 and average 0.42 (Table 1), which is typical of magmatic zircon (Belousova et al., 2002). The $^{206}Pb/^{238}U$ ages of the ten zircon crystals analyzed vary from 149 to 156 Ma and yield a weighted mean $^{206}Pb/^{238}U$ age of 152.8 ± 1.2 Ma (MSWD = 1.6) (Fig. 9). This age is interpreted to represent the crystallization age of the Laiziling granite.

Garnet petrography, chemical composition and LA-ICP-MS U-Pb ages

Three types of garnet were identified using BSE images and an optical microscope (Fig. 7). Crystals of Type I garnet (Grt-I; e.g., sample 19XHL-45-1) are euhedral, brown to yellow in color, homogeneous and between 0.5 and 1.0 mm in diameter. This garnet type is overgrown by Type II garnet (Grt-II) (Fig. 7A, B), which is lighter than Grt-I (from light brown yellow to grayish white) and also homogeneous, but more abundant (0.5 to 3.0 mm in diameter) (Fig. 7A - E). Type II garnet coexists with diopside, both of which were replaced by fluorite (Fig. 7B). Type III garnet (Grt-III) is grayish white (Fig. 7D), homogeneous and has a prismatic morphology (~2 mm × 300 µm). It is interspersed with Grt-II (Fig. 7D, E). No cassiterite was found in these samples.

Electron microprobe analyses show that the three types of garnets have similar chemical compositions (Table 2). Their main components are SiO_2 (35.69 wt%), CaO (33.06 wt%), Al_2O_3 (15.86 wt%) and FeO^T (5.93 wt%); the values in parentheses are their average concentrations. The three types of garnet are members of the grossular-andradite solid solution series; they are grossular-rich (73.09-76.92 mol%) and contain minor pyralspite (the sum of pyrope, spessartine, almandine and uvarovite; < 8.0 mol%) (Table 2; Fig. 7F).

The results of the LA-ICP-MS U-Pb analyses for the garnet samples are summarized in Appendix Table 1. The Grt-I, Grt-II and Grt-III yielded Tera-Wasserburg concordia intercept ages of 153.6 ± 7.6 Ma (MSWD = 1.3; n = 58; Fig. 10A), 153.0 ± 17 Ma (MSWD = 1.7; n = 85; Fig. 10B) and 151.5 ± 3.5 Ma (MSWD = 1.3; n = 59; Fig. 10C), respectively.

Cassiterite petrography and LA-ICP-MS U-Pb ages

Four types of cassiterite were distinguished from the different ore types (Fig. 8). Type I cassiterite occurs as disseminations in the proximal skarn-type ore (Cst I, e.g., sample 19XHL-10-6). This cassiterite type has been subdivided into early (Cst I-1) and late (Cst I-2) stages. The Cst I-1 crystals are dark brown, anhedral and homogeneous, and occur as irregular aggregates, in which the individual crystals vary from 50 to 600 μm in diameter (Fig. 5C, 8A). The Cst I-1 variety was replaced by Cst I-2, a bright luminescing variety, which fills embayments and fractures in Cst I-1 (Fig 8B). Type I cassiterite is accompanied by actinolite, wollastonite, muscovite, quartz and pyrrhotite (Fig. 5C, 8B, C). Type II cassiterite occurs as disseminations in the distal skarn-type ore (Cst II, e.g., sample 19XHL-3). The Cst II variety is light brown, anhedral with a diameter of ~100 um (Fig. 8D). Parts of crystals display zoning patterns in CL images (Fig. 8E). This cassiterite is commonly associated with actinolite, quartz, pyrrhotite, and chalcopyrite (Fig. 8D, F). Type III cassiterite is disseminated in the cassiterite-sulfide vein ore (Cst III, e.g., sample 19XHL-17-1 and 19XHL-24). The Cst III variety is light yellow brown and occurs as euhedral crystals with a diameter of 1000-1500 μm (Fig. 5G, 8G). It displays weak oscillatory zoning in CL images (Fig. 8H) and is commonly associated with arsenopyrite, pyrrhotite, fluorite, muscovite and quartz (Fig. 5H, 8G, H, I). Type IV cassiterite occurs in the distal Sn-Pb-Zn veinlet ore (Cst IV, e.g., sample ZK7003-11). As is the case for Cst I, there were two stages of Cst IV development, Cst IV-1 and Cst IV-2. The Cst IV-1 cassiterite is represented by brown, euhedral crystals 500-700 μm in diameter (Fig. 8J). It displays color zoning under both plane polarized transmitted light (Fig. 8J) and in CL images (Fig. 8K). The edges of early Cst IV-1 crystals were replaced by Cst IV-2, which also fills cracks in Cst IV-1 (Fig. 8K). The Cst IV variety coexists with pyrite, arsenopyrite, galena, sphalerite, topaz, and quartz (Fig. 4C, 5I, J, K, 8L).

The results of LA-ICP-MS U-Pb analyses of the cassiterite samples are summarized in Appendix Table 2. The Cst I-1 sample (34 spots for sample 19XHL-10-6) yielded a Tera-Wasserburg concordia intercept age of 155.4 ± 0.8 Ma (MSWD = 3.3; Fig. 11D). The Cst II sample (39 spots for sample 19XHL-3) yielded a Tera-Wasserburg concordia intercept age of 155.9 ± 0.7 Ma (MSWD = 1.4; Fig. 11E). Two Cst III samples (26 spots for sample 19XHL-17-1 and 22 spots for sample 19XHL-24) yielded Tera-Wasserburg concordia intercept ages of 154.2 ± 0.9 (MSWD = 2.1; Fig. 11F) and 152.3 ± 1.1 Ma (MSWD =3.5; Fig. 11G), respectively. Two Cst IV-1 crystals from sample ZK7003-11 yielded Tera-Wasserburg concordia intercept ages of 159.3 ± 1.5 (MSWD = 0.66; Fig. 11A) and 158.5 ± 0.8 Ma (MSWD = 1.7; Fig. 11B), respectively. Forty-one spots of Cst IV-2 yielded a Tera-Wasserburg concordia intercept age of 159.6 ± 1.4 Ma (MSWD = 2.6; Fig. 11C).

DISCUSSION

Reliability of garnet and cassiterite U-Pb geochronology

Minerals suitable for robust geochronology are commonly absent from skarns (Deng et al., 2017) and consequently, the age data for them are often acquired from minerals not directly related to skarn formation. This makes interpretation of the ages ambiguous (Yuan et al., 2011; Li et al., 2019; Marfin et al., 2020). Mezger et al. (1989) recognized the potential of garnet as a U-Pb geochronometer firstly because of the variable U contents and a high closure temperature of U-Pb isotopes (>800°C). However, garnet from magmatic and hydrothermal conditions usually contains a variety of U-rich mineral inclusions and, thus, may pose problems for U-Pb geochronological analysis (Dewolf et al., 1996; Lima et al., 2012). Such problems can be solved by in situ analytical techniques (Liu et al., 2010). Higher U and lower common Pb concentrations have been shown to be important for obtaining more accurate garnet U-Pb ages (Deng et al., 2017; Gevedon et al., 2018; Li D et al., 2018, 2019; Hong et al., 2022). Li et al. (2019) concluded that the U concentration should be >1 ppm and the ^{204}Pb content should be <10% of the U concentration when using the ICP-MS. Garnet with a variety of U concentrations has been successfully applied to date hydrothermal ore deposits. Examples include the Shuiquangou Au deposit (U = 0.11 to 20.30 ppm, Deng et al., 2017), the Haobugao Zn-Pb-Sn deposit (U = 0.54 to 5.32 ppm, Hong et al., 2021), the Big Gossan Cu-Au deposit (U = 0.50 to 199.90 ppm, Wafforn et al., 2018), and the Pingbao Pb-Zn district (U = 1.11 to 579.00 ppm, Li et al., 2019). The U concentrations of the Xianghualing garnet vary from 1 to 114 ppm (Appendix Table 1), which enables this mineral to produce robust geochronological data.

Cassiterite (SnO_2), the main tin ore mineral, is common in skarn-type, greisen-type and other type tin deposits (Gulson and Jones, 1992; Yuan et al., 2011). It is characterized by relatively high U contents, stable chemical properties and a high closure temperature for U-Pb isotope system (this temperature can reach 560°C for a 1 μm diameter crystal and 860°C for a 1mm diameter crystal; Zhang et al., 2011). Therefore, cassiterite U-Pb geochronology can constrain the timing of tin mineralization accurately and directly, making cassiterite the most ideal dating mineral for tin deposits (Gluson and Jones, 1992; Zhang et al., 2015; Neymark et al., 2018, 2021). Isotope dilution-thermal ionization mass spectrometry (ID-TIMS) and laser ablation inductively coupled plasma-mass spectrometry (LA-ICP-MS) cassiterite U-Pb dating techniques have been developed to constrain tin mineralization events (Gluson and Jones, 1991, Yuan et al., 2008, 2011; Neymark et al., 2018), and LA-ICP-MS techniques are now widely applied to obtain reliable ages of tin deposits (Zhang et al., 2015, 2017a, b; Guo et al., 2019, Xiong et al., 2020). Studies have also shown that cassiterite U-Pb geochronology can be used to identify multiple mineralization events (Zhang et al., 2015; Xiong et al., 2020). Therefore, a combination of the two geochronological methods mentioned above could help to identify the timing of both skarn formation and Sn mineralization directly.

Discrete mineralization events at Xianghualing

The Xianghualing tin deposit consists not only of proximal Sn skarn ores, but also of distal Sn skarn ores and Sn-Pb-Zn veinlets. Whether the distal Sn skarn ores and Sn-Pb-Zn veinlets are genetically related to the proximal skarn mineralization, i.e., whether both were products of the Laiziling magmatic-hydrothermal system, however, has been unclear due to the lack of precise geochronological data for the different Sn ore stages.

The zircon U-Pb age of the Laiziling granite obtained in this study is 152.8 ± 1.2 Ma (Fig. 9B). Based on this and previously determined ages, the Laiziling granite is interpreted to have been intruded between ~156 and 150 Ma (e.g., biotite K-Ar method, Hu et al., 1984; zircon U-Pb method, Liu, 2011; Zhu et al., 2011; Lai, 2014; Li H et al., 2018; Yang et al., 2018; Xiao et al., 2019). Yuan et al. (2008) and Guo et al. (2019) dated cassiterite from a cassiterite-arsenopyrite-pyrrhotite vein in the Xinfeng ore block and the Laiziling granite, respectively, and obtained U-Pb ages for them of 156 ± 4 and 149.0 ± 1.8 Ma, respectively. These previous geochronological studies did not consider the skarn-type mineralization, and ignored the temporal relationships between the distal Sn-Pb-Zn veinlets, skarn mineralization, and the intrusion.

In this study, we have reported garnet U-Pb ages for the prograde skarn (153.6 ± 7.6 to 151.5 ± 3.5 Ma, Fig. 10) and U-Pb ages of cassiterite (155.9 ± 0.7 to 155.4 ± 0.8 Ma, Fig. 11D, E) from proximal and distal retrograde skarn ores. These age data record the timing of skarn formation and skarn-hosted Sn mineralization and show that the events were essentially coeval with the emplacement of the Laiziling pluton. We have also shown from the ages of two cassiterite-arsenopyrite-pyrrhotite veins, which we dated at 154.2 ± 0.9 and 152.3 ± 1.1 Ma (Fig. 11F, G), that this mineralization was also coeval with the emplacement of the Laiziling granite and associated skarn mineralization (Fig. 12). As a result, we have been able to establish the temporal evolution for the Sn mineralizing system produced by the Laiziling granite, i.e., from the emplacement of Laiziling granite (152.8 ± 1.2 Ma), prograde skarn alteration (153.6 ± 7.6 to 151.5 ± 3.5 Ma), to tin mineralization in retrograde skarn and the cassiterite-sulfide stage (155.9 ± 0.7 to 152.3 ± 1.1 Ma).

The ages obtained in this study for the distal Sn-Pb-Zn veinlet Sn mineralization

(159.6 ± 1.4 to 158.5 ± 0.8 Ma, Fig. 11A-C) show that there was a tin mineralizing event in the Xianghualing ore district that preceded emplacement of the Laiziling pluton (Fig. 12). As there is W-Sn-Pb-Zn mineralization (161.3 ± 1.1 and 158.7 ± 1.2 Ma, muscovite Ar-Ar, Yuan et al., 2007) around the Jianfengling granitic intrusion, which is located ~4 km laterally from the Laiziling pluton (Fig. 1C) and zircon U-Pb ages of 165.2 ± 1.4 to 160.7 ± 2.2 Ma have been reported for the Jianfengling intrusion (Xuan et al., 2014, Yang et al., 2018), we attribute the distal Sn-Pb-Zn veinlets to the Jianfengling intrusion. We therefore conclude that there were two Sn mineralizing events in the Xianghualing ore field, an early event represented by distal Sn-Pb-Zn veinlet mineralization related to the Jianfengling intrusion and a subsequent skarn-type Sn mineralizing event related to the Laiziling intrusion (Fig. 12).

Owing to their similar geochemical characteristics and an age difference of ~10 Ma, less attention has been paid to mineralization between the Laiziling and Jianfengling plutons (Xuan et al., 2014; Yang et al., 2018). Previous studies have shown that the two plutons may have originated from the same magma chamber (Yang et al., 2018). Regional geophysical data suggest that the two plutons are connected at depth (Lai, 2014; Zhong, 2014), raising the possibility of earlier (~165-160 Ma) magmatism in the Laiziling pluton. Therefore, we speculate that a hidden granitic intrusion coeval with the Jianfengling granite intrusion was responsible for the early Sn mineralizing event in the Xianghualing deposit (Fig. 13). The results of our study show that there were two episodes of tin mineralization at Xianghualing, i.e., at ~160 Ma (Sn I) and 156-150 Ma (Sn II), and that these episodes were related to the magmas that formed the Jianfengling granite and Laiziling granite, respectively.

Significance for regional Sn mineralization

In the Xianghualing deposit, the early mineralization event (~160 Ma) only accounts for ≤ 5% of the total Sn resource, and the younger main Sn mineralization event (156-150 Ma) contributes ~>95% of the total Sn resource. Previous studies have shown that formation of the Sn deposits in the Nanling Range was relatively continuous from the Silurian to the Cretaceous, and concluded that the period between 160 and 150 Ma was a time of major W-Sn mineralization (Chen et al., 2013; Mao et al., 2013; Yuan et al., 2019). We have roughly calculated the total Sn reserve emplaced in the Nanling Range between 160 and 150 Ma to be 2.78 Mt, which accounts for ~80% of the total Sn reserves in this area (3.27 Mt, Cao et al., 2015, Yuan et al., 2019). Among them, the Sn reserves introduced at ~160 Ma are 1.02 Mt (Furong with 0.70 Mt, Hehuaping with 0.2 Mt, and Jinchuantang with 0.12 Mt, Yuan et al., 2019 and references therein), whereas the Sn reserves introduced between 156 and 150 Ma amount to 1.56 Mt (Shizhuyuan with 0.80 Mt, Xitian with 0.59 Mt, and Xianghualing with 0.17 Mt, Yuan et al., 2019 and references therein). Therefore, we can infer that ~160 Ma and 156-150 Ma were both major periods of Sn mineralization in the Nanling Range.

In summary, a new genetic model involving two discrete Sn mineralizing events is proposed to explain the Sn mineralization of Xianghualing district (Fig. 13). This model provides an important new guide for tin ore exploration in the Xianghualing district and the Nanling Range, generally, i.e., the targeting of skarn- and cassiterite-sulfide vein-type orebodies related to the emplacement of ~160 Ma intrusions and superimposed cassiterite mineralization introduced by the 156-150 Ma magmatic-hydrothermal system.

IMPLICATIONS

The new cassiterite and garnet LA-ICP-MS U-Pb ages coupled with field observations and core-logging lead to the conclusion that there were two tin mineralization events in the Xianghualing ore district, South China. The early event occurred between 159.6 ± 1.4 and 158.5 ± 0.8 Ma based on cassiterite U-Pb geochronology, and was likely caused by a hidden granitic intrusion coeval with the nearby Jianfengling intrusion. This event only accounts for ≤5% of the total tin resource. The main Sn mineralization event occurred between 155.9 ± 0.7 and 152.3 ± 1.1 Ma based on cassiterite and garnet LA-ICP-MS U-Pb ages, and is genetically related to the Laiziling granitic intrusion (zircon U-Pb age of 152.8 ± 1.2 Ma). This event contributed >95% of the total tin resources. Our new geochronological results provide evidence of a superimposed tin mineralizing system in the Xianghualing ore district, a finding that is of great significance to the regional tin exploration. This study demonstrates the reliability of cassiterite and garnet U-Pb geochronology in identifying discrete tin mineralizing events in complex metallogenic systems.

ACKNOWLEDGMENTS AND FUNDING

This study was financially supported by the National Natural Science Foundation of China (Grants 42122012 and 92062219), the National Key R&D Program of China (Grant 2018YFC0603901), the Fundamental Research Funds for the Central Universities (Grants QZ05201904, 2652018169), and the 111 Project of the Ministry of Science and Technology (BP0719021). We thank the leaders and employees of the Xianghualing tin Industry Co., Ltd. for their wholehearted support during the field investigation. We appreciate Hongyu Zhang, Yubo Yang, Huan Wang, and Can Rao for their help during the analysis. We thank Donald W. Davis and Ryan Mathur for their insightful reviews, which considerably improved this paper. Associate Editor Daniel Gregory is thanked for his editorial help and useful suggestions.

REFERENCES

Baker, T., Achterberg, E.V., Ryan, C.G., and Lang, J.R. (2004) Composition and evolution of ore fluids in a magmatic-hydrothermal skarn deposit. Geology, 32, 117-120.

Belousova, E.A., Griffin, W.L., O'Reilly, S.Y., and Fisher, N.I. (2002) Igneous zircon: Trace element composition as an indicator of source rock type. Contributions to Mineralogy and Petrology, 143, 602-622.

Cao, H.W. (2015) Research on Mesozoic-Cenozoic magmatic evolution and its relation with metallogeny in Tengchong-Lianghe tin ore belt, Westen Yunnan. China University of Geosciences (Beijing), 1-349 (in Chinese with English abs.).

Chang, Z.S., Shu, Q.H., and Meinert, L.D. (2019) Skarn deposits of China. Society of

Economic Geologists, Special Publication, 22, 189-234.

Chen, J., Wang, R.C., Zhu, J.C., Lu, J.J., and Ma, D.S. (2013) Multiple-aged granitoids and related tungsten-tin mineralization in the Nanling Range, South China. Science China: Earth Sciences, 56, 2045-2055.

Chen, J.F., and Jahn, B. (1998) Crustal evolution of southeastern China: Nd and Sr isotopic evidence. Tectonophysics, 284, 101-133.

Chen, L.L., Ni, P., Dai, B.Z., Li, W.S., Chi, Z., and Pan, J.Y. (2019) The genetic association between quartz vein-and greisen-type mineralization at the Maoping W–Sn Deposit, Southern Jiangxi, China: Insights from zircon and cassiterite U–Pb ages and cassiterite trace element composition. Minerals, 9, 411.

Chiaradia, M., Schaltegger, U., Spikings, R., Wotzlaw, J.F., and Ovtcharova, M. (2013) How accurately can we date the duration of magmatic-hydrothermal events in porphyry systems? —An invited paper. Economic Geology, 108, 565-584.

Chiaradia, M., Vallance, J., Fontboté, L., Stein, H., Schaltegger, U., Coder, J., Richards, J., Villeneuve, M., and Gendall, I. (2009) U-Pb, Re-Os, and $^{40}Ar/^{39}Ar$ geochronology of the Nambija Au-skarn and Pangui porphyry Cu deposits, Ecuador: Implications for the Jurassic metallogenic belt of the Northern Andes. Mineralium Deposita, 44, 371-387.

Davis, D.W., Williams, I.S., and Krogh, T.E. (2003) Historical development of zircon geochronology. Reviews in Mineralogy and Geochemistry, 53 (1), 145-181.

Deng, X.D., Li, J.W., Luo, T., and Wang, H.Q. (2017) Dating magmatic and hydrothermal processes using andradite-rich garnet U–Pb geochronometry. Contributions to Mineralogy and Petrology, 172, 1-11.

DeWolf, C.P., Zeissler, C.J., Halliday, A.N., Mezger, K., and Essene, E.J. (1996) The role of inclusions in U-Pb and Sm-Nd garnet geochronology: Stepwise dissolution experiments and trace uranium mapping by fission track analysis. Geochimica et Cosmochimica Acta, 60, 121-134.

Fu, J.M., Li, H.Q., Qu, W.J., Yang, X.J., Wei, J.Q., Liu, G.Q., and Ma, L.Y. (2007) Re-Os isotope dating of the Da'ao tungsten-tin deposit in the Jiuyi Mountains, southern Hunan Province: Geology in China, 34, 651-656 (in Chinese with English abs.).

Gevedon, M., Seman, S., Barnes, J.D., Lackey, J.S., and Stockli, D.F. (2018) Unraveling histories of hydrothermal systems via U-Pb laser ablation dating of skarn garnet. Earth and Planetary Science Letters, 498, 237-246.

Gulson, B.L., and Jones, M.T. (1992) Cassiterite: potential for direct dating of mineral-deposits and a precise age for the Bushveld complex granites. Geology, 20, 355-358.

Guo, B.E., Zhao, K.D., Jiang, S.Y., and Chen, W. (2019) Genetic relationship between Laiziling rare metal granite and No. 431 dyke and mechanism of Sn-Nb-Ta mineralization, Southern Hunan Province. Abstract of the 9th National Symposium on metallogenic Theory and Prospecting Methods, p. 131 (in Chinese with English abs.).

Hong, J.X., Zhang, H.Y., Li, D.F., Ouyang, Y.P., Zhai, D.G., Liu, F., and Liu, J.J.

(2022) In situ LA-ICP-MS U-Pb geochronology and geochemical characteristics of garnet from the Zhuxi skarn W-Cu deposit, South China. Ore Geology Reviews, 140, 104577.

Hong, J.X., Zhang, H.Y., Zhai, D.G., Li, D.F., Zhang, Y.L., and Liu, J.J. (2021) The geochronology of the Haobugao skarn Zn-Pb deposit (NE China) using garnet LA-ICP-MS U-Pb dating. Ore Geology Reviews, 139, 104437.

Hoskin, P.W.O., and Schaltegger U. (2003) The composition of zircon and igneous and metamorphic petrogenesis. Reviews in Mineralogy and Geochemistry, 53, 27-62.

Hu, Y.J., Huang, R.M., and Gong, M.Y. (1984) Two lead-zinc deposits of endogenetic metal metallogenic series in Southern Hunan Province. Hunan Geology, 3, 1-13 (in Chinese with English abs.).

Hua, R.M., Chen, P.R., Zhang, W.L., Yao, J.M. (2005) Metallogenesis related to Mesozoic granitoids in the Nanling Range, South China and their geodynamic settings. Acta Geologica Sinica, 79, 810-820.

Jia, H.X., Pang, Z.S., Chen, R.Y., Xue, J.L., Chen, H., and Lin, L.J. (2018) Genesis and hydrothermal evolution of the Tiantangshan tin-polymetallic deposit, south-eastern Nanling Range, South China. Geological Journal, 1-22.

Jiang, W.C., Li, H., Eans, N.J., Wu, J.H., and Cao, J.Y. (2018) Metal sources of world-class polymetallic W–Sn skarns in the Nanling Range, South China: Granites versus sedimentary rocks? Minerals, 8, 265.

Lai, S.H. (2014) Research on Mineralization of the Xianghualing tin polymetallic deposit, Hunan Province, China. China University of Geosciences (Beijing), p. 1-151 (in Chinese with English abs.).

Li, D.F., Fu, Y., Hollings, P., Mitchell, R.H., Zurevinski, S., Kamo, S., Zhang, R.Q., Zhang, Y., Liu, Q.F., Liao, J.L., Liang, Y.J., and Sun, X.M. (2022) PL57 garnet as a new natural reference material for in situ U-Pb isotope analysis and its perspective for geological applications, Contributions to Mineralogy and Petrology, 177: 19.

Li, D.F., Fu, Y., and Sun, X.M. (2018) Onset and duration of Zn-Pb mineralization in the Talate Pb-Zn (-Fe) skarn deposit, NW China: Constraints from spessartine U-Pb dating. Gondwana Research, 63, 117-128.

Li, D.F., Tan, C.Y., Miao, F.Y., Liu, Q.F., Zhang, Y., and Sun, X.M. (2019) Initiation of Zn-Pb mineralization in the Pingbao Pb-Zn skarn district, South China: Constraints from U-Pb dating of grossular-rich garnet. Ore Geology Reviews, 107, 587-599.

Li, H., Wu, J.H., Evans, N.J., Jiang, W.C., and Zhou, Z.K. (2018) Zircon geochronology and geochemistry of the Xianghualing A-type granitic rocks: Insights into multi-stage Sn-polymetallic mineralization in South China. Lithos, 312-313, 1-20.

Li, Q., Zhao, K.D., Lai, P.C., Jiang, S.Y., and Chen, W. (2018) Petrogenesis of Cretaceous volcanic-intrusive complex from the giant Yanbei tin deposit, South China: Implication for multiple magma sources, tin mineralization, and geodynamic setting. Lithos, 296-299, 163-180.

Li, X.H., Li, W.X., Li, Z.X., and Liu, Y. (2008) 850–790 Ma bimodal volcanic and intrusive rocks in northern Zhejiang, South China: a major episode of continental rift magmatism during the breakup of Rodinia. Lithos, 102, 341-357.

Li, X.H., Tang, G.Q., Gong, B., Yang, Y.H., Hou, K.J., Hu, Z.C., Li, Q.L., Liu. Y., and Li, W.X. (2013) Qinghu zircon: A working reference for microbeam analysis of U-Pb age and Hf and O isotopes. Chinese Science Bulletin, 58, 1954-1961 (in Chinese with English abs.).

Li, Z.X., Li, X.H., Zhou, H., and Kinny, P.D. (2002) Grenvillian continental collision in south China: new SHRIMP U-Pb zircon results and implications for the configuration of Rodinia. Geology, 30, 163-166.

Lima, S.M., Corfu, F., Neiva, M.R., and Ramos, J.M.F. (2012) U-Pb ID-TIMS dating applied to U-rich inclusions in garnet. American Mineralogist, 97, 800-806.

Liu, Y. (2011) Crust-mantle interaction of Yanshanian granitic magma in Qitianling and Daoxian area southern Hunan. Chinese Academy of Geological Science, p. 1-296 (in Chinese with English abs.).

Liu, Y.S., Hu, Z.C., Zong, K.Q., Gao, C.G., Gao, S., Xu, J. and Chen, H.H. (2010) Reappraisement and refinement of zircon U-Pb isotope and trace element analyses by LA-ICP-MS. Chinese Science Bulletin, 55, 1535-1546.

Ludwig, K.R. (2003) User's manual for Isoplot 3.0: a geochronological toolkit for Microsoft Excel, Special Publication 4. Geochronology Center, Berkeley.

Mao, J.W., Cheng, Y.B., Chen, M.H., and Pirajno, F. (2013) Major types and time-space distribution of Mesozoic ore deposits in South China and their geodynamic settings. Mineralium Deposita, 48, 267-294.

Mao, J.W., Pirajno, F., and Cook, N. (2011) Mesozoic metallogeny in East China and corresponding geodynamic settings — An introduction to the special issue. Ore Geology Reviews, 43, 1-7.

Marfin, A.E., Ivanov, A.V., Kamenetsky, V.S., Abersteiner, A., Yakich, T.Y., and Dudkin, T.V (2020) Contact metamorphic and metasomatic processes at the Kharaelakh intrusion, Oktyabrsk deposit, Norilsk-Talnakh ore district: Application of Laser Ablation-Inductively Coupled Plasma-Mass Spectrometry dating of perovskite, apatite, garnet, and titanite. Economic Geology, 115, 1213-1226.

Mathur, R., Titley, S., Ruiz, J., Gibbins, S., and Friehauf, K. (2005) A Re-Os isotope study of sedimentary rocks and copper-gold ores from the Ertsberg District, West Papua, Indonesia. Ore Geology Reviews, 26, 207-226.

Mei, W., Lü, X.B., Cao, X.F., Liu, Z., Zhao, Y., Ai, Z.L., Tang, R.K., and Abfaua, M.M. (2014) Ore genesis and hydrothermal evolution of the Huanggang skarn iron-tin polymetallic deposit, southern Great Xing'an Range: Evidence from fluid inclusions and isotope analyses. Ore Geology Reviews, 64, 239-252.

Meinert, L.D., Hefton, K.K., Mayes, D., and Tasiran, I. (1997) Application of skarn deposit zonation models to mineral exploration. Exploration and Mining Geology, 6, 185-208.

Meinert, L.D., Dipple, G.M., and Nicolescu, S. (2005) World skarn deposits, In: Hedenquist, J.W., Thompson, J.F.H., Goldfarb, R.J., Richards, J.P. (Eds.), Economic Geology 100th Anniversary Volume, 1905–2005, Society of Economic Geologists Inc, Littleton, Colorado, p. 299-336.

Meffre, S., Large, R.R., Scott, R., Woodhead, J., Chang, Z., Gilbert, S.E., Danyushevsky, L.V., Maslennikov, V., and Hergt, J.M. (2008) Age and pyrite Pb-isotope composition of the giant Sukhoi Log sediment-hosted gold deposit, Russia: Geochimica et Cosmochimica Acta, 72, 2377-2391.

Mezger, K., Hanson, G., and Bohlen, S. (1989) U-Pb systematics of garnet: dating the growth of garnet in the Late Archean Pikwitonei granulite domain at Cauchon and Natawahunan Lakes, Manitoba, Canada. Contributions to Mineralogy and Petrology, 101, 36-148.

Newberry, R.J., Einaudi, M.T., and Eastman, H.S. (1991) Zoning and genesis of the Darwin Pb-Zn-Ag skarn deposit, California: A reinterpretation based on new data. Economic Geology, 86, 960-982.

Neymark, L.A., Holm-Denoma, C.S., and Moscati, R.J. (2018) In situ LA-ICPMS U–Pb dating of cassiterite without a knownage matrix-matched reference material: Examples from worldwide tin deposits spanning the Proterozoic to the Tertiary. Chemical Geology, 483, 410-425.

Neymark, L.A., Holm-Denoma, C.S., Larin, A.M., Moscati, R.J., and Plotkina, Y.V. (2021) LA-ICPMS U-Pb dating reveals cassiterite inheritance in the Yazov granite, Eastern Siberia: Implications for tin mineralization. Mineralium Deposita, 56, 1177-1194.

Pearce, N.J.G., Perkins, W.T., Westgate, J.A., Gorton, M.P., Jackson, S.E., Neal, C.R., and Chenery, S.P. (1997) A compilation of new published major and trace element data for NIST SRM 610 and NIST SRM 612 glass reference materials. Geostandards and Geoanalytical Research, 21, 114-115.

Petrus, J.A. and Kamber, B.S. (2012) VizualAge: Anovel approach to laser ablation ICP-MS U-Pb geochronology data reduction. Geostandards and Geoanalytical Research, 36(3): 247-270.

Prichard, J. (2013) The geochemistry and geochronology of cassiterite from the New England Fold Belt: NSW. BSC honours thesis, Australian National University.

Shu, X.J., Wang X.L., Sun, T., Xu, X.S., and Dai, M.N. (2011) Trace elements, U-Pb ages and Hf isotopes of zircons from Mesozoic granites in the western Nanling Range, South China: Implications for petrogenesis and W-Sn mineralization. Lithos, 127, 468-482.

Sillitoe, R.H. (2010) Porphyry Copper Systems. Economic Geology, 105, 3-41.

Sun, W.D., Yang, X.Y., Fan, W.M., and Wu, F.Y. (2012) Mesozoic large scale magmatism and mineralization in South China: Preface. Lithos, 150, 1-5.

Tapster, S. and Bright, J.W.G. (2020) High-precision ID-TIMS cassiterite U-Pb systematics using a low-contamination hydrothermal decomposition: implications for LA-ICP-MS and ore deposit geochronology. Geochronology, 2, 425-441.

Vermeesch, P. (2018) IsoplotR: A free and open toolbox for geochronology. Geoscience Frontiers, 9, 1479-1493.

Wafforn, S., Seman, S., Kyle, J.R., Stockli, J.R., Leys, C., Sonbait, D., and Cloos, M.

(2018) Andradite garnet U-Pb geochronology of the Big Gossan skarn, Ertsberg-Grasberg mining district, Indonesia. Economic Geology, 113, 769-778.

Wang, Y.J., Fan, W.M., Zhang, G.W., and Zhang, Y.H. (2013) Phanerozoic tectonics of the South China Block: Key observations and controversies. Gondwana Research, 23, 1273-1350.

Wiedenbeck, M., Allé, P., Corfu, F., Griffin, W.L., Meier, M., Oberli, F., Quadt, A. Von, Roddick, J.C., and Spiegel, W. (1995) Three natural zircon standards for U-Th-Pb, Lu-Hf, trace element and REE analyses. Geostandards Newsletter,19, 1-23.

Williams-Jones, A.E., Samson, I.M., Ault, K.M., Gagnon, J.E., and Fryer, B.J. (2010) The genesis of distal zinc skarns: evidence from the Mochito deposit, Honduras. Economic Geology, 105, 1411-1440.

Wu, J.H., Li, H., Algeo, T.J., Jiang, W.C., and Zhou, Z.K. (2018) Genesis of the Xianghualing Sn–Pb–Zn deposit, South China: A multimethod zircon study. Ore Geology Reviews, 102, 220-239.

Wu, S.H., Mao, J.W., Yuan, S.D., Dai, P., and Wang, X.D. (2018) Mineralogy, fluid inclusion petrography, and stable isotope geochemistry of Pb-Zn-Ag veins at the Shizhuyuan deposit, Hunan Province, southeastern China. Mineralium Deposita, 53, 89-103.

Xiao, C.H., Shen, Y.K., and Wei, C.S. (2019) Petrogenesis of low Sr and high Yb A-type granitoids in the Xianghualing Sn polymetallic deposit, South China: Constrains from geochronology and Sr–Nd–Pb–Hf isotopes. Minerals, 9, 182.

Xie, L., Wang, Z.J., Wang, R.C., Zhu, J.C., Che, X.D., Gao, J.F., and Zhao, X. (2018) Mineralogical constraints on the genesis of W-Nb-Ta mineralization in the Laiziling granite (Xianghualing district, south China). Ore Geology Reviews, 95, 695-712.

Xiong, X.L., Rao, B., Chen, F.R., Zhu, J.C., and Zhao, Z.H. (2002) Crystallization and melting experiments of a fluorine-rich leucogranite from the Xianghualing pluton, South China, at 150 MPa and H_2O-saturated conditions. Journal of Asian Earth Sciences, 21, 175-188.

Xiong, Y.Q., Shao, Y.J., Cheng, Y.B., and Jiang, S.Y. (2020) Discrete Jurassic and Cretaceous mineralization events at the Xiangdong W(-Sn) deposit, Nanling Range, South China. Economic Geology, 115, 385-413.

Xuan, Y.S., Yuan, S.D., Yuan, Y.B., and Mi, J.R. (2014) Zircon U-Pb age, geochemistry and petrogenesis of Jianfengling pluton in southern Hunan Province. Mineral Deposits, 33, 1379-1390 (in Chinese with English abs.).

Yang, L.Z., Wu, X.B., Cao, J.Y., Hu, B., Zhang, X.W., Gong, Y.S., and Liu, W.D. (2018) Geochronology, petrology, and genesis of two granitic plutons of the Xianghualing ore field in South Hunan Province: Constraints from zircon U–Pb dating, geochemistry, and Lu–Hf isotopic compositions. Minerals, 8, 213.

Yu, X.G., Rao, C., Wang, W.M.Y., Lin, X.Q., and Tan, L.Q. (2018) Mineralogical behavior and metallogenic process of Sn in the Xianghualing skarn, Hunan Province: Geological Journal of China Universities, 24, 645-657 (in Chinese with English abs.).

Yuan, S.D, Williams-Jones, A.E., Romer, R.L., Zhao, P.L., and Mao, J.W. (2019) Protolith-related thermal controls on the decoupling of Sn and W in Sn-W metallogenic provinces: Insights from the Nanling Region, China. Economic Geology, 114, 1005-1012.

Yuan, S.D., Mao, J.W., Cook, N.J., Wang, X.D., Liu, X.F., and Yuan, Y.B. (2015) A Late Cretaceous tin metallogenic event in Nanling W–Sn metallogenic province: Constraints from U–Pb, Ar–Ar geochronology at the Jiepailing Sn–Be–F deposit, Hunan, China. Ore Geology Reviews, 65, 283-293.

Yuan, S.D., Peng, J. T., Shen, N. P., Hu, R. Z., and Dai, T.M. (2007) ^{40}Ar-^{39}Ar isotopic dating of the Xianghualing Sn-polymetallic orefield in southern Hunan, China and its geological implications. Acta Geologica Sinica, 81, 278-286.

Yuan, S.D., Peng, J.T, Hu, R.Z., Li, H.M., Shen, N.P., and Zhang, D.L. (2008) A precise U–Pb age on cassiterite from the Xianghualing tin-polymetallic deposit (Hunan, South China). Mineralium Deposita, 43, 375-382.

Yuan, S.D., Peng, J.T., Hao, S., Li, H.M., Geng, J.Z., and Zhang, D.L. (2011) In situ LA-MC-ICP-MS and ID-TIMS U-Pb geochronology of cassiterite in the giant Furong tin deposit, Hunan Province, south China: New constraints on the timing of tin-polymetallic mineralization. Ore Geology Reviews, 43, 235-242.

Yudintsev, S.V., Lapina, M.I., Ptashkin, A.G., Ioudintseva, T.S., Utsunomiya, S., Wang, L.M., and Ewing, R.C. (2002) Accommodation of Uranium into the Garnet structure. Materials Research Society, 713, JJ11.28.

Zhai, D.G., Liu, J.J., Zhang, A.L., Sun, Y.Q. (2017) U-Pb, Re-Os, and ^{40}Ar-^{39}Ar

geochronology of porphyry Sn ± Cu ± Mo and polymetallic (Ag-Pb-Zn-Cu) vein mineralization at Bianjiadayuan, Inner Mongolia, Northeast China: Implications for discrete mineralization events. Economic Geology, 112, 2041-2059.

Zhai, D.G., Liu, J.J., Zhang, H.Y., Yao, M.J., Wang, J.P., and Yang, Y.Q. (2014) S-Pb isotopic geochemistry, U-Pb and Re-Os geochronology of the Huanggangliang Fe-Sn deposit, Inner Mongolia, NE China. Ore Geology Reviews, 59, 109-122.

Zhai, D.G., Williams-Jones, A.E., Liu, J.J., David, S., Li, C., Huang, X.W., Qi, L., and Guo, D.H. (2019) Evaluating the use of the molybdenite Re-Os chronometer in dating gold mineralization: Evidence from the Haigou deposit, NE China. Economic Geology, 114(5), 897-915.

Zhang, D.L., Peng, J.T., Hu, R.Z., Yuan, S.D., and Zheng, D.S., 2011, The closure of U-Pb isotope system in cassiterite and its reliability for dating: Geological Review, 57, 549-554 (in Chinese with English abs.).

Zhang, R.Q., Lehmann, B., Seltmann, R., Sun, W.D., and Li, C. (2017a) Cassiterite U-Pb geochronology constrains magmatic-hydrothermal evolution in complex evolved granite systems: The classic Erzgebirge tin province (Saxony and Bohemia). Geology, 45, 1095-1098.

Zhang, R.Q, Lu, J.J., Wang, R.C., Yang, P., Zhu, J.C., Yao, Y., Gao, J.F., Li, C., Lei, Z.H., Zhang, W.L., and Guo, W.M. (2015) Constraints of in situ zircon and cassiterite U–Pb, molybdenite Re–Os and muscovite ^{40}Ar–^{39}Ar ages on multiple generations of granitic magmatism and related W–Sn mineralization in the

Wangxianling area, Nanling Range, South China. Ore Geology Reviews, 65, 1021-1042.

Zhang, R.Q., Lu, J.J., Lehmann, B., Li, C.Y., Li, G.L., Zhang, L.P., Guo, J., and Sun, W.D. (2017b) Combined zircon and cassiterite U-Pb dating of the Piaotang granite-related tungsten-tin deposit, southern Jiangxi tungsten district, China. Ore Geology Reviews, 82, 268-284.

Zhang, S.T., Chen, H.Y., Shu, Q.H., Zhang, Y., Chu, G.B., Cheng, J.M., and Tian, J. (2019) Unveiling growth histories of multi-generational garnet in a single skarn deposit via newly-developed LA-ICP-MS U-Pb dating of grandite. Gondwana Research, 73, 65-76.

Zhao, P.L., Yuan, S.D., Mao, J.W., Yuan, Y.B., Zhao, H.J., Zhang, D.L., and Shuang, Y. (2018) Constraints on the timing and genetic link of the large-scale accumulation of proximal W–Sn–Mo–Bi and distal Pb–Zn–Ag mineralization of the world-class Dongpo orefield, Nanling Range, South China. Ore Geology Reviews, 95, 1140-1160.

Zhao, Q.Q., Zhai, D.G., Mathur, R., Liu, J.J., Selby, D., and Williams-Jones, A.E. (2021) The giant Chalukou porphyry Mo deposit, NE China: The product of a short-lived, high flux mineralizing event. Economic Geology, 116 (5), 1209-1225.

Zhong, J.L. (2014) Major types and prospecting direction of nonferrous and rare polymetallic ore deposit in Xianghualing area, South China. Geology and Mineral Resources of South China, 30, 99-108 (in Chinese with English abs.).

Zhou, X.M., and Li, W.X (2000) Origin of Late Mesozoic igneous rocks in Southeastern China: implications for lithosphere subduction and underplating of mafic magmas. Tectonophysics, 326, 269-287.

Zhou, X.M., Sun, T., Shen, W.Z., Shu, L.S., and Niu, Y.L. (2006) Petrogenesis of Mesozoic granitoids and volcanic rocks in South China: A response to tectonic evolution. Episodes, 29, 26-33.

Zhu, J.C., Wang, R.C., Lu, J.J., Zhang, H., Zhang, W.L., Xie, L., and Zhang, R.Q. (2011) Fractionation, evolution, petrogenesis and mineralization of Laiziling granite pluton, Southern Hunan Province. Geological Journal of China Universities, 17, 381-392 (in Chinese with English abs.).

FIGURE CAPTIONS

FIGURE 1. (A) A tectonic map of China (Xiong et al., 2020); (B) The distribution of granite and associated tungsten-tin deposits in the Nanling Range (modified after Chen et al., 2013 and Yuan et al., 2019); (C) A regional geological map of the Xianghualing ore field (modified after Yuan et al., 2007 and Wu J et al., 2018).

FIGURE 2. A geological map of the Xianghualing Sn deposit (modified after Wu J et al., 2018).

FIGURE 3. The vertical zonation of rock types in the Laiziling pluton (A) (Xiong et al., 2002) and metal zoning of the Xianghualing tin deposit (B) (Lai, 2014).

FIGURE 4. Geological cross sections of No. 49 exploration line in the Xinfeng ore block (A) (Wu J et al., 2018), No. 88 exploration line in the Tangguanpu ore block (B) (Lai, 2014) and (C) the distribution of Sn-Pb-Zn mineralization in drill hole of ZK7003 in the Tangguanpu ore block.

FIGURE 5. Photographs showing different ore types for the Xianghuaing Sn deposit. (A) The contact between biotite granite and marble in the 580 m level tunnel of the Tangguanpu ore block; (B) Massive skarn-type ore; (C) Actinolite associated with biotite and cassiterite in proximal skarn ore (plane polarized light); (D) Biotite granite; (E) Granular quartz and sericitized K-feldspar in biotite granite (crossed polarized light); (F) Distal skarn ore at the contact zone between Devonian sandstone and Cambrian sandstone; (G) Disseminated arsenopyrite and cassiterite in a cassiterite-sulfide vein; (H) The assemblage cassiterite-arsenopyrite-pyrrhotite-chalcopyrite-fluorite (reflected light); (I) Sn-Pb-Zn veinlets in the drill core of ZK6601 in the Tangguanpu ore block; (J) Sn-Pb-Zn veinlets in the drill core of ZK7003 in the Tangguanpu ore block, containing coexisting pyrite and galena (reflected light); (K) The coexistence of cassiterite, arsenopyrite, and topaz in Sn-Pb-Zn veinlets (plane polarized light). Abbreviations: Act = actinolite, Apy = arsenopyrite, Bi = biotite, Ccp = chalcopyrite, Cst = cassiterite, Di = diopside, Fl = fluorite, Gn = galena, Grt = garnet, Kfs = K-feldspar, Pl = plagioclase, Po = pyrrhotite, Qtz = quartz, Sp = sphalerite, Tpz = topaz.

FIGURE 6. The paragenetic sequence of minerals in the Xianghualing tin deposit.

FIGURE 7. Photomicrographs and backscattered electron (BSE) images for garnet from the

Xianghualing tin deposit. (A) Stage I garnet hosted in Stage II garnet (plane polarized light); (B) Stage I garnet replaced by Stage II garnet, both of which were replaced by fluorite (BSE); (C) Stage II garnet intergrown with diopside (BSE); (D) Granular Stage II garnet replaced by tabular Stage III garnet (plane polarized light); (E) Granular Stage II garnet replaced by tabular Stage III garnet (BSE); (F) A ternary diagram illustrating the composition of the Xianghualing garnet. Abbreviations: Alm = almandine, And = andradite, Ep = epidote, Gro = grossular, Pyr = pyrope, Spe = spessartine and Uva = uvarovite (modified after Meinert et al., 2005).

FIGURE 8. Photomicrographs and cathodoluminescence (CL) images for cassiterite from the Xianghualing tin deposit. (A) Cassiterite (Cst I) in close association with actinolite in proximal skarn ore (plane polarized light); (B) Relatively dark cassiterite (Cst I-1) in proximal skarn ore replaced by late light colored cassiterite (Cst I-2) (CL); (C) Cassiterite (Cst I) intergrown with actinolite and pyrrhotite in proximal skarn ore (reflected light); (D) Cassiterite (Cst II) coexisting with actinolite and quartz in distal skarn ore (plane polarized light); (E) Cassiterite (Cst II) grains in distal skarn ore (CL); (F) Cassiterite (Cst II) intergrown with pyrrhotite and chalcopyrite in distal skarn ore (reflect light); (G) Cassiterite (Cst III) in cassiterite-sulfide ore with growth zones replaced by muscovite (plane polarized light); (H) Cassiterite in cassiterite-sulfide ore (Cst III) showing growth zones (CL); (I) Cassiterite (Cst III) in contact with pyrrhotite and arsenopyrite in cassiterite-sulfide ore (reflected light); (J) Cassiterite (Cst IV) displaying growth zones surrounded by topaz in a Sn-Pb-Zn veinlet (plane polarized light); (K) Dark cassiterite (Cst IV-1) in a Sn-Pb-Zn veinlet showing growth zones and filled and later cassiterite (Cst IV-2) along cracks (CL); (L) Cassiterite (Cst IV) intergrown with arsenopyrite, pyrite, galena, and topaz (reflected light).

Abbreviations: Act = actinolite, Apy = arsenopyrite, Cst = cassiterite, Fl = fluorite, Gn = galena, Ms = muscovite, Po = pyrrhotite, Qtz = quartz, Tpz = topaz.

FIGURE 9. (A) Cathodoluminescence (CL) images of representative zircon crystals separated from the Laiziling granite showing the locations of the analyses (circles) and corresponding U-Pb ages; (B) A concordia diagram and weighted mean age of zircon crytals from sample 19XHL-12 of the Laiziling granitic pluton.

FIGURE 10. Tera-Wasserburg U-Pb intercept ages for garnet in the Xianghualing Sn deposit. (A) Euhedral garnet (Grt-I); (B) Granular garnet (Grt-II); (C) Tabular garnet (Grt-III).

FIGURE 11. Tera-Wasserburg U-Pb intercept ages for cassiterite in the Xianghualing Sn deposit. (A) The U-Pb age for dark cassiterite (Cst IV-1) in a Sn-Pb-Zn veinlet ore from sample ZK7003-11; (B) The U-Pb age for a second cassiterite crystal (Cst IV-1) from sample ZK7003-11; (C)The U-Pb age of the the late light colored cassiterite (Cst IV-2) from sample ZK7003-11; (D) The U-Pb age for dark cassiterite (Cst I) in proximal skarn ore from sample 19XHL-10-6; (E) The U-Pb age for cassiterite (Cst II) in distal skarn ore from sample 19XHL-3; (F) The U-Pb age for cassiterite (Cst III) in cassiterite-sulfide ore from sample 19XHL-17-1; (G) The U-Pb age for cassiterite (Cst III) in cassiterite-sulfide ore from sample 19XHL-24.

FIGURE 12. A diagram illustrating the distribution of age determinations for the Jianfengling and Laiziling granites and the early and late Sn mineralizing events in the Xianghualing ore field. The

zircon U-Pb ages are from Liu, 2011; Shu et al., 2011; Zhu et al., 2011; Lai, 2014; Xuan et al., 2014; Li H et al., 2018; Yang et al., 2018; Xiao et al., 2019; the muscovite Ar-Ar ages are from Hu et al., 1984; Yuan et al., 2007; and the cassiterite U-Pb ages are from Yuan et al., 2008a; Guo et al., 2019 and this study.

FIGURE 13. A proposed genetic model for Sn mineralization in the Xianghualing ore district.

TABLES

TABLE 1. LA-ICP-MS U-Pb data for zircon in the Laiziling granitic pluton

TABLE 2. A summary of the major element compositions of the Xianghualing garnet (wt%)

APPENDIX TABLES

APPENDIX TABLE 1. LA-ICP-MS U-Pb isotope data for garnet from the Xianghualing Sn deposit

APPENDIX TABLE 2. LA-ICP-MS U-Pb isotope data for cassiterite from the Xianghualing Sn deposit

APPENDIX TABLE 3. LA-ICP-MS U-Pb isotope data for garnet standards GRT-1 and WS-20

DOI: https://doi.org/10.2138/am-2022-8412. http://www.minsocam.org/

Table 1. LA-ICP-MS U-Pb data for zircons in the Laiziling granitic pluton

Sample	Contents (ppm)			Th/U	Isotopic ratios						Ages (Ma)					
					$^{207}Pb/^{206}Pb$		$^{207}Pb/^{235}U$		$^{206}Pb/^{238}U$		$^{207}Pb/^{206}Pb$		$^{207}Pb/^{235}U$		$^{206}Pb/^{238}U$	
	Pb	Th	U		Ratio	1σ	Ratio	1σ	Ratio	1σ	Ratio	1σ	Ratio	1σ	Ratio	1σ
XHL12-01	11.85	222.20	421.81	0.53	0.04929	0.00205	0.16602	0.00680	0.02442	0.00030	162	73	156	6	156	2
XHL12-04	29.23	768.02	986.27	0.78	0.04921	0.00151	0.16423	0.00492	0.02420	0.00028	158	48	154	4	154	2
XHL12-09	17.62	277.16	655.97	0.42	0.04917	0.00172	0.16309	0.00559	0.02405	0.00029	156	58	153	5	153	2
XHL12-22	37.68	529.21	1379.38	0.38	0.05620	0.00177	0.18830	0.00582	0.02430	0.00029	460	47	175	5	155	2
XHL12-34	70.96	803.52	2769.62	0.29	0.05902	0.00198	0.19540	0.00641	0.02401	0.00030	568	50	181	5	153	2
XHL12-36	253.36	1958.49	7211.36	0.27	0.05612	0.00567	0.18112	0.01815	0.02341	0.00032	457	231	169	16	149	2
XHL12-46	270.14	3055.95	9845.57	0.31	0.05420	0.00299	0.17634	0.00946	0.02360	0.00031	379	128	165	8	150	2
XHL12-48	174.69	2393.32	6016.88	0.40	0.04773	0.00285	0.15665	0.00912	0.02380	0.00031	86	133	148	8	152	2
XHL12-50	25.36	510.24	895.70	0.57	0.05091	0.00344	0.16795	0.01109	0.02393	0.00034	237	155	158	10	152	2
XHL12-52	163.32	1785.43	6333.59	0.28	0.05138	0.00184	0.17075	0.00601	0.02410	0.00032	258	56	160	5	154	2

Table 2. A summary of the major element compositions of the Xianghualing garnets (wt%)

Sample	19XHL-45	19XHL-45	19XHL-45	19XHL-45	19XHL-45	19XHL-18-1	19XHL-18-	19XHL-45	19XHL-18-1	19XHL-18-1	19XHL-18-1
	GrtI-1	GrtI-2	Grt II-1	Grt II-2	Grt II-3	Grt II-4	Grt II-5	Grt III-1	Grt III-2	Grt III-3	Grt III-4
SiO_2	35.94	35.59	37.63	38.31	38.03	34.37	34.37	33.51	35.07	35.96	33.81
TiO_2	1.04	0.83	0.68	0.78	1.88	1.17	0.70	2.62	1.23	1.17	1.30
Al_2O_3	15.38	15.73	17.76	18.07	16.81	15.21	14.30	14.68	15.04	15.83	15.70
Cr_2O_3	0.02	0.00	0.00	0.01	0.00	0.03	0.00	0.00	0.03	0.03	0.00
Fe_2O_3	0.00	0.00	0.00	0.00	0.00	0.00	0.00	0.00	0.00	0.00	0.00
FeO	6.09	5.51	7.04	6.98	7.23	4.98	5.24	5.30	5.96	5.06	5.88
MnO	0.25	0.25	1.63	1.56	1.58	0.27	0.26	0.30	0.27	0.24	0.19

DOI: https://doi.org/10.2138/am-2022-8412. http://www.minsocam.org/

MgO	1.77	1.76	0.16	0.18	0.07	1.52	1.68	1.19	1.71	1.69	1.39
CaO	34.20	34.33	32.69	33.16	33.21	31.66	31.01	31.69	33.97	34.32	33.40
Total	94.68	94.00	97.59	99.05	98.81	89.20	87.56	89.29	93.27	94.32	91.66
Si	2.92	2.91	2.96	2.97	2.96	2.94	3.00	2.88	2.90	2.92	2.84
Ti	0.06	0.05	0.04	0.05	0.11	0.08	0.05	0.17	0.08	0.07	0.08
Al	1.47	1.52	1.65	1.65	1.54	1.54	1.47	1.49	1.46	1.52	1.56
Cr	0.00	0.00	0.00	0.00	0.00	0.00	0.00	0.00	0.00	0.00	0.00
Fe^{3+}	0.41	0.38	0.35	0.34	0.41	0.36	0.38	0.38	0.41	0.34	0.41
Fe^{2+}	0.00	0.00	0.11	0.11	0.06	0.00	0.00	0.00	0.00	0.00	0.00
Mn	0.02	0.02	0.11	0.10	0.10	0.02	0.02	0.02	0.02	0.02	0.01
Mg	0.21	0.21	0.02	0.02	0.01	0.19	0.22	0.15	0.21	0.21	0.17
Ca	2.98	3.01	2.76	2.75	2.77	2.91	2.90	2.92	3.01	2.99	3.01
And	19.33	17.44	17.56	17.10	21.22	17.15	18.27	18.48	19.09	16.08	19.40
Gro	73.40	75.39	74.44	75.02	73.09	75.88	74.16	75.87	73.73	76.92	74.72
Pyr+Spe+Alm+Uva	7.27	7.17	8.00	7.87	5.69	6.98	7.57	5.65	7.17	7.01	5.88

Note: Total Fe are measured and represented as FeO. All the calculations were based on 12 oxygens. Abbreviation: Alm = almandine; And = andradite; Gro = grossular; Pyr = pyrope; Spe = spessartine; and Uva = uvarovite.

Fig. 1

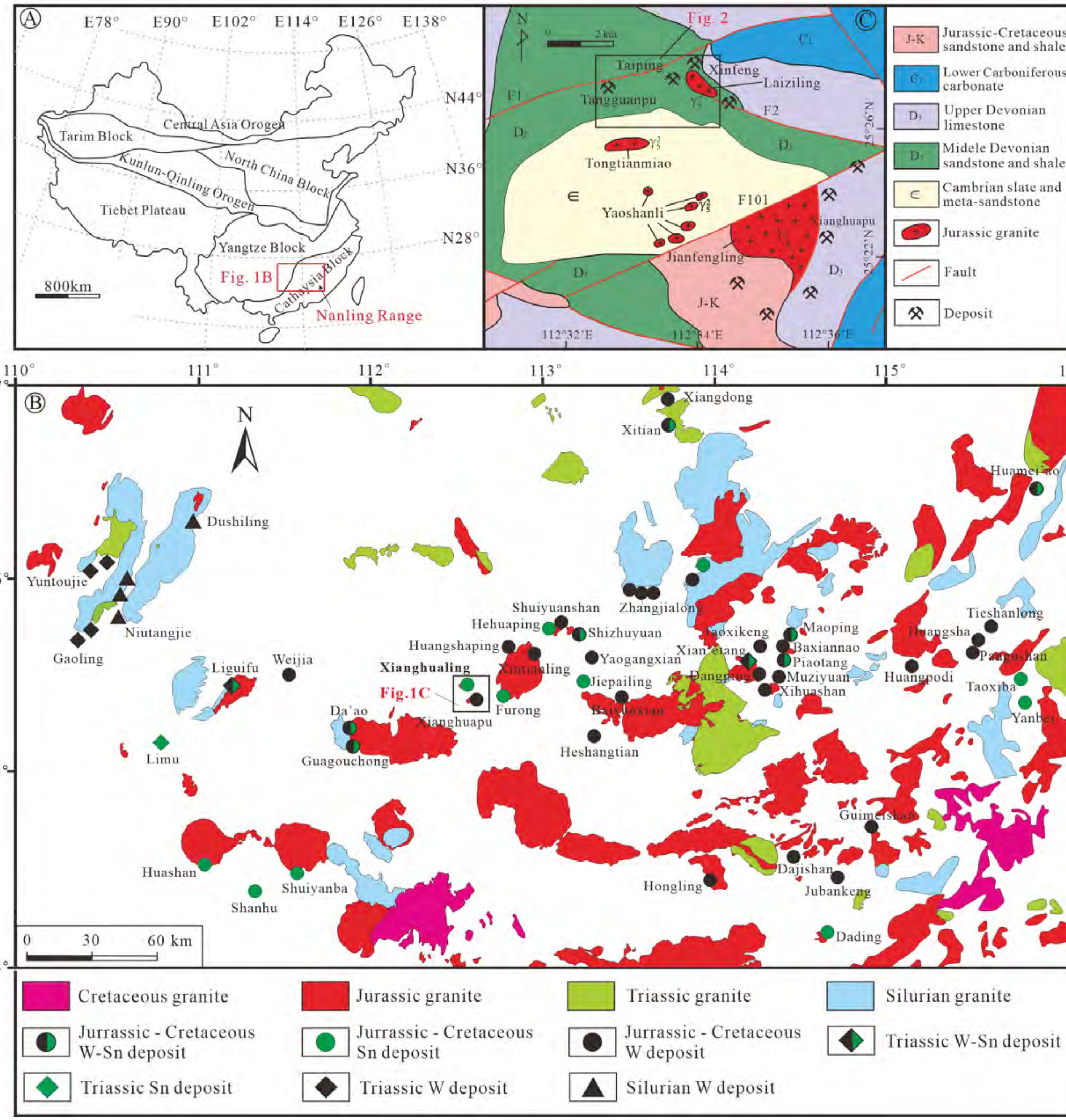
Tarim Block
Central Asia Orogen
North China Block
Kunlun-Qinling Orogen
Tiebet Plateau
Yangtze Block
Cathaysia Block
Fig. 1B
Nanling Range
800km
Fig. 2
Taiping
Xinfeng
Laiziling
Tangguanpu
Tongtianmiao
Yaoshanli
F101
Xianghuapu
Jianfengling
Jurassic-Cretaceous sandstone and shale
Lower Carboniferous carbonate
Upper Devonian limestone
Midele Devonian sandstone and shale
Cambrian slate and meta-sandstone
Jurassic granite
Fault
Deposit
Xiangdong
Xitian
Dushiling
Yuntoujie
Niutangjie
Gaoling
Liguifu
Weijia
Limu
Xianghualing
Fig.1C
Xianghuapu
Da'ao
Guagouchong
Furong
Huangshaping
Hehuaping
Shuiyuanshan
Shizhuyuan
Yaogangxian
Jiepailing
Heshangtian
Zhangjialong
Maoping
Baxiannao
Piaotang
Muziyuan
Xihuashan
Huangsha
Tieshanlong
Huangpodi
Taoxiba
Yanbei
Huamei'ao
Guimeishan
Dajishan
Jubankeng
Hongling
Dading
Huashan
Shuiyanba
Shanhu
0 30 60 km
Cretaceous granite
Jurassic granite
Triassic granite
Silurian granite
Jurrassic - Cretaceous W-Sn deposit
Jurrassic - Cretaceous Sn deposit
Jurrassic - Cretaceous W deposit
Triassic W-Sn deposit
Triassic Sn deposit
Triassic W deposit
Silurian W deposit

This is the peer-reviewed, final accepted version for American Mineralogist, published by the Mineralogical Society of America.
The published version is subject to change. Cite as Authors (Year) Title. American Mineralogist, in press.
DOI: https://doi.org/10.2138/am-2022-8412. http://www.minsocam.org/

Fig. 2

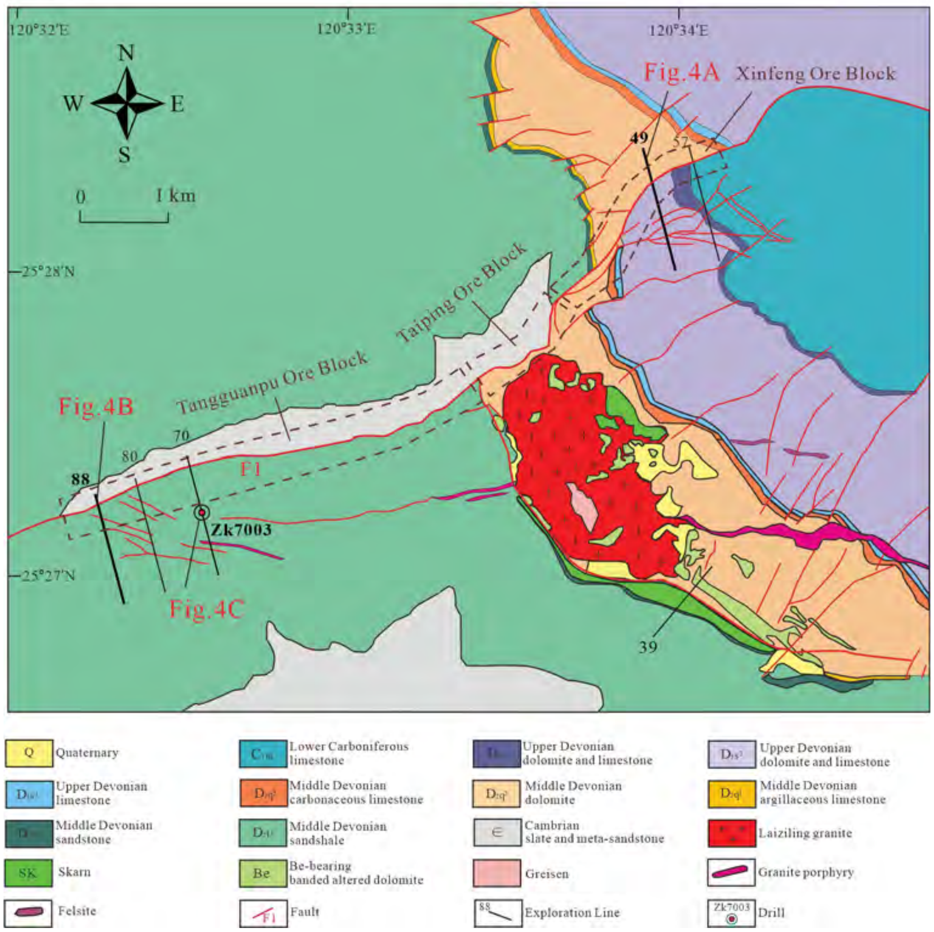

Fig. 3

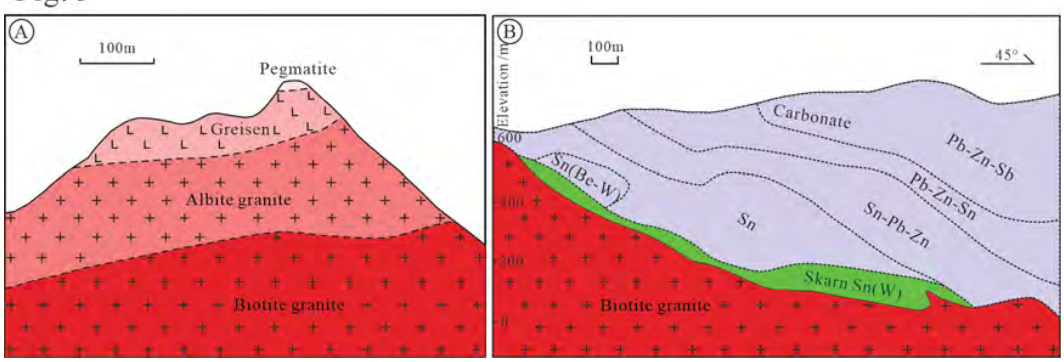
A
100m
Pegmatite
Greisen
Albite granite
Biotite granite
B
Elevation /m
100m
45°
600
400
200
0
Carbonate
Pb-Zn-Sb
Pb-Zn-Sn
Sn-Pb-Zn
Sn(Be-W)
Sn
Skarn Sn(W)
Biotite granite

Fig. 4

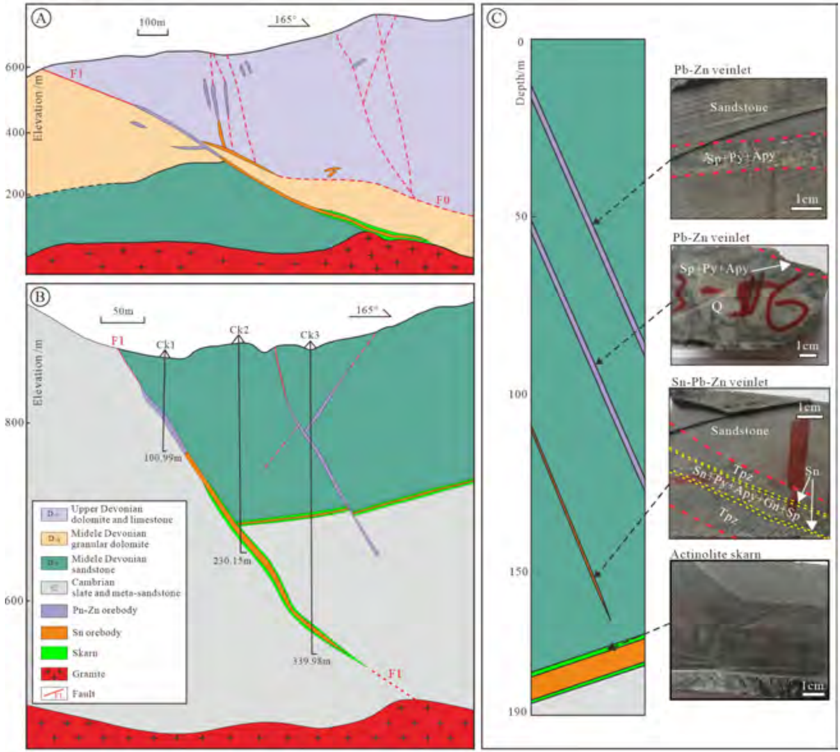
A
100m
165°
600
400
200
Elevation /m
F1
F0
B
50m
165°
F1
Ck1
Ck2
Ck3
Elevation /m
800
600
100.99m
230.15m
339.98m
F1
Upper Devonian dolomite and limestone
Midele Devonian granular dolomite
Midele Devonian sandstone
Cambrian slate and meta-sandstone
Pb-Zn orebody
Sn orebody
Skarn
Granite
Fault
C
Depth/m
0
50
100
150
190
Pb-Zn veinlet
Sandstone
Sp+Py+Apy
1cm
Pb-Zn veinlet
Sp+Py+Apy
Q
1cm
Sn-Pb-Zn veinlet
1cm
Sandstone
Tpz
Sn+Py+Apy+Gn+Sp
Sn
Tpz
Actinolite skarn
1cm

Fig. 5

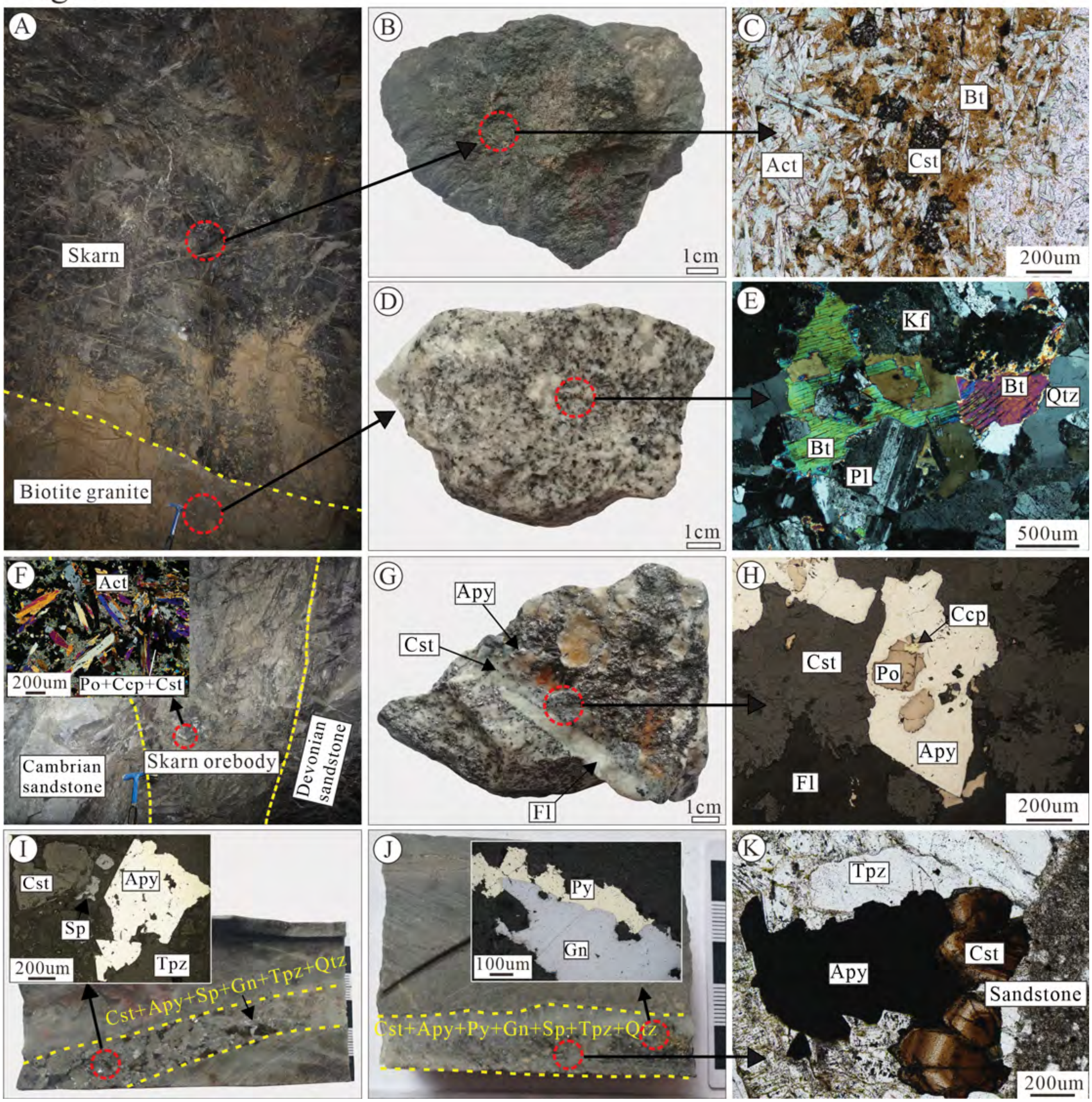
A
Skarn
Biotite granite
B
1cm
C
Bt
Act
Cst
200um
D
1cm
E
Kf
Bt
Qtz
Bt
Pl
500um
F
Act
200um
Po+Ccp+Cst
Cambrian sandstone
Skarn orebody
Devonian sandstone
G
Apy
Cst
Fl
1cm
H
Ccp
Cst
Po
Apy
Fl
200um
I
Cst
Apy
Sp
Tpz
200um
Cst+Apy+Sp+Gn+Tpz+Qtz
J
Py
Gn
100um
Cst+Apy+Py+Gn+Sp+Tpz+Qtz
K
Tpz
Apy
Cst
Sandstone
200um

Fig. 6

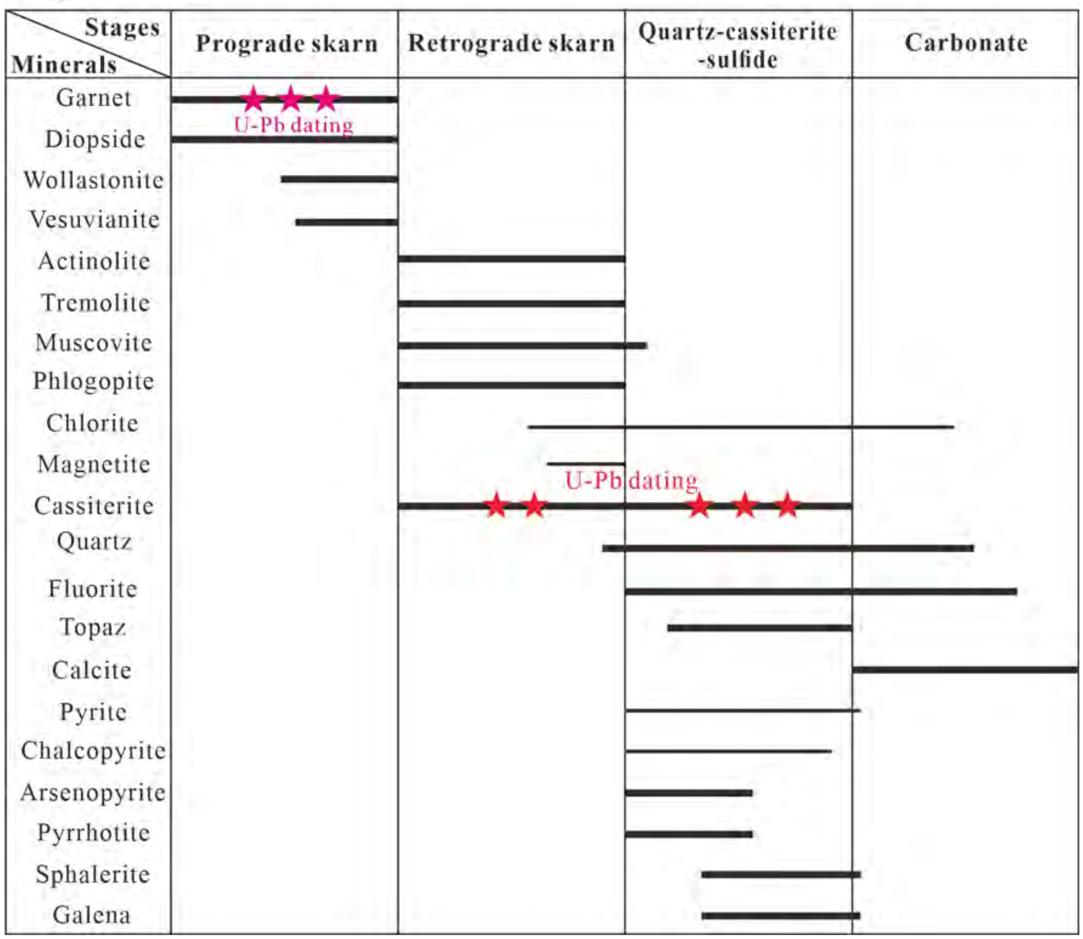
Stages
Minerals
Prograde skarn
Retrograde skarn
Quartz-cassiterite -sulfide
Carbonate
Garnet
Diopside
Wollastonite
Vesuvianite
Actinolite
Tremolite
Muscovite
Phlogopite
Chlorite
Magnetite
Cassiterite
Quartz
Fluorite
Topaz
Calcite
Pyrite
Chalcopyrite
Arsenopyrite
Pyrrhotite
Sphalerite
Galena
U-Pb dating
U-Pb dating

Fig.7

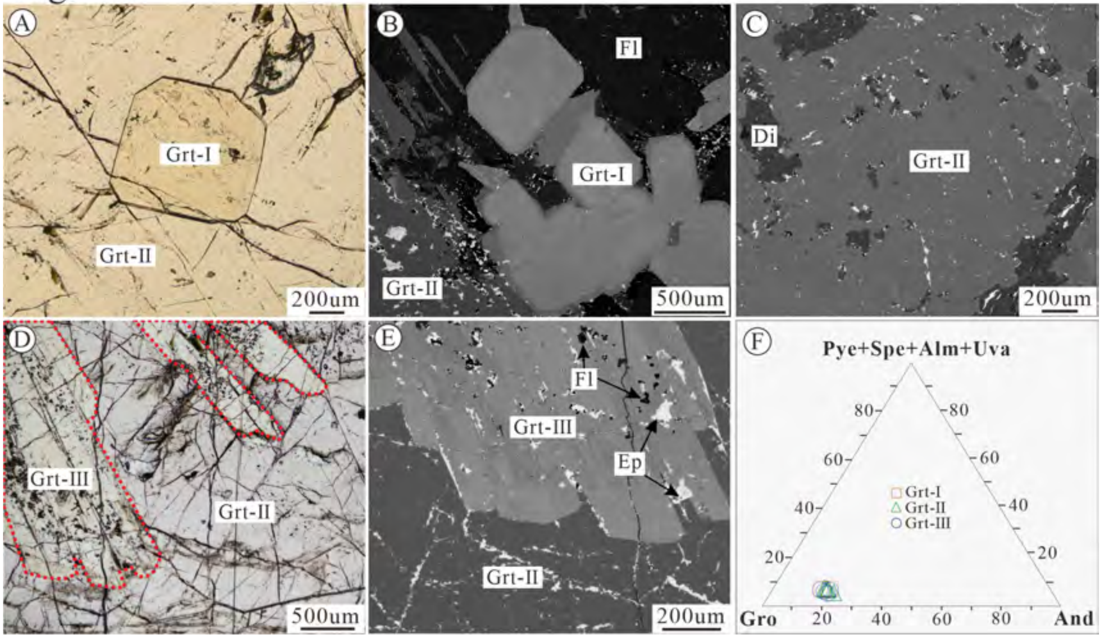
A
Grt-I
Grt-II
200um
B
Fl
Grt-I
Grt-II
500um
C
Di
Grt-II
200um
D
Grt-III
Grt-II
500um
E
Fl
Grt-III
Ep
Grt-II
200um
F
Pye+Spe+Alm+Uva
Grt-I
Grt-II
Grt-III
Gro
And
20
40
60
80

Fig. 8

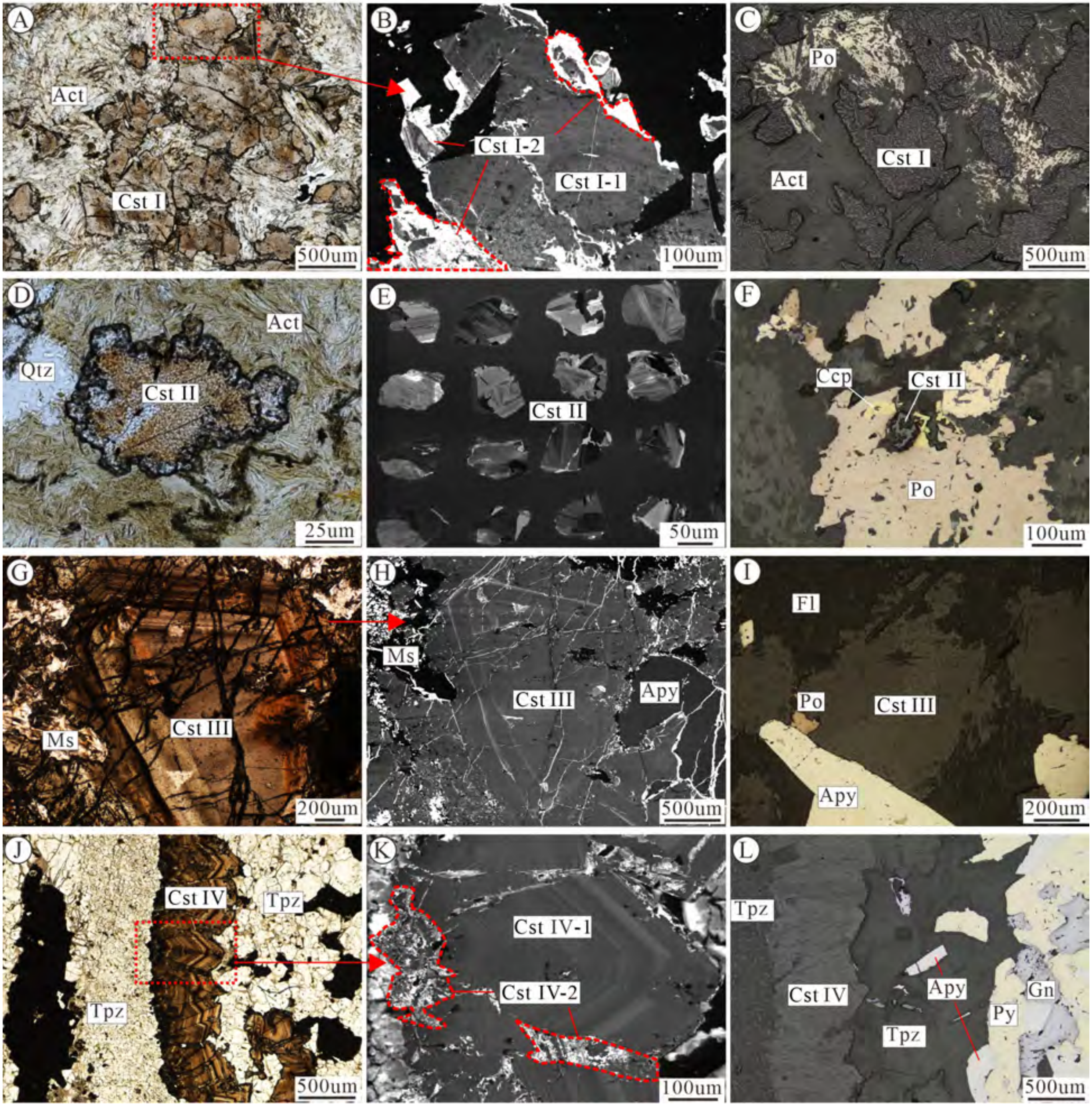
A
Act
Cst I
500um
B
Cst I-2
Cst I-1
100um
C
Po
Cst I
Act
500um
D
Act
Qtz
Cst II
25um
E
Cst II
50um
F
Ccp
Cst II
Po
100um
G
Ms
Cst III
200um
H
Ms
Cst III
Apy
500um
I
Fl
Po
Cst III
Apy
200um
J
Cst IV
Tpz
Tpz
500um
K
Cst IV-1
Cst IV-2
100um
L
Tpz
Cst IV
Apy
Gn
Py
Tpz
500um

Fig. 9

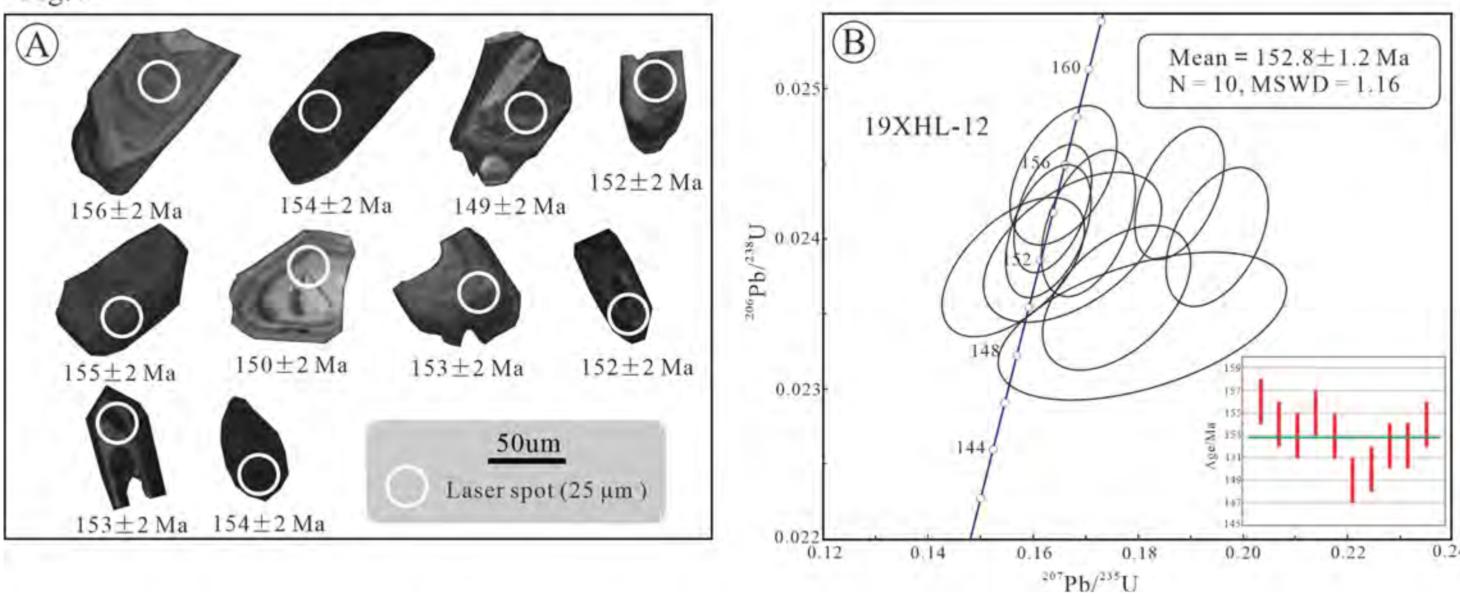
A
156±2 Ma
154±2 Ma
149±2 Ma
152±2 Ma
155±2 Ma
150±2 Ma
153±2 Ma
152±2 Ma
153±2 Ma
154±2 Ma
50um
Laser spot (25 μm)
B
Mean = 152.8±1.2 Ma
N = 10, MSWD = 1.16
19XHL-12
160
156
152
148
144
0.025
0.024
0.023
0.022
0.12
0.14
0.16
0.18
0.20
0.22
0.24
206Pb/238U
207Pb/235U
Age/Ma

Fig. 10

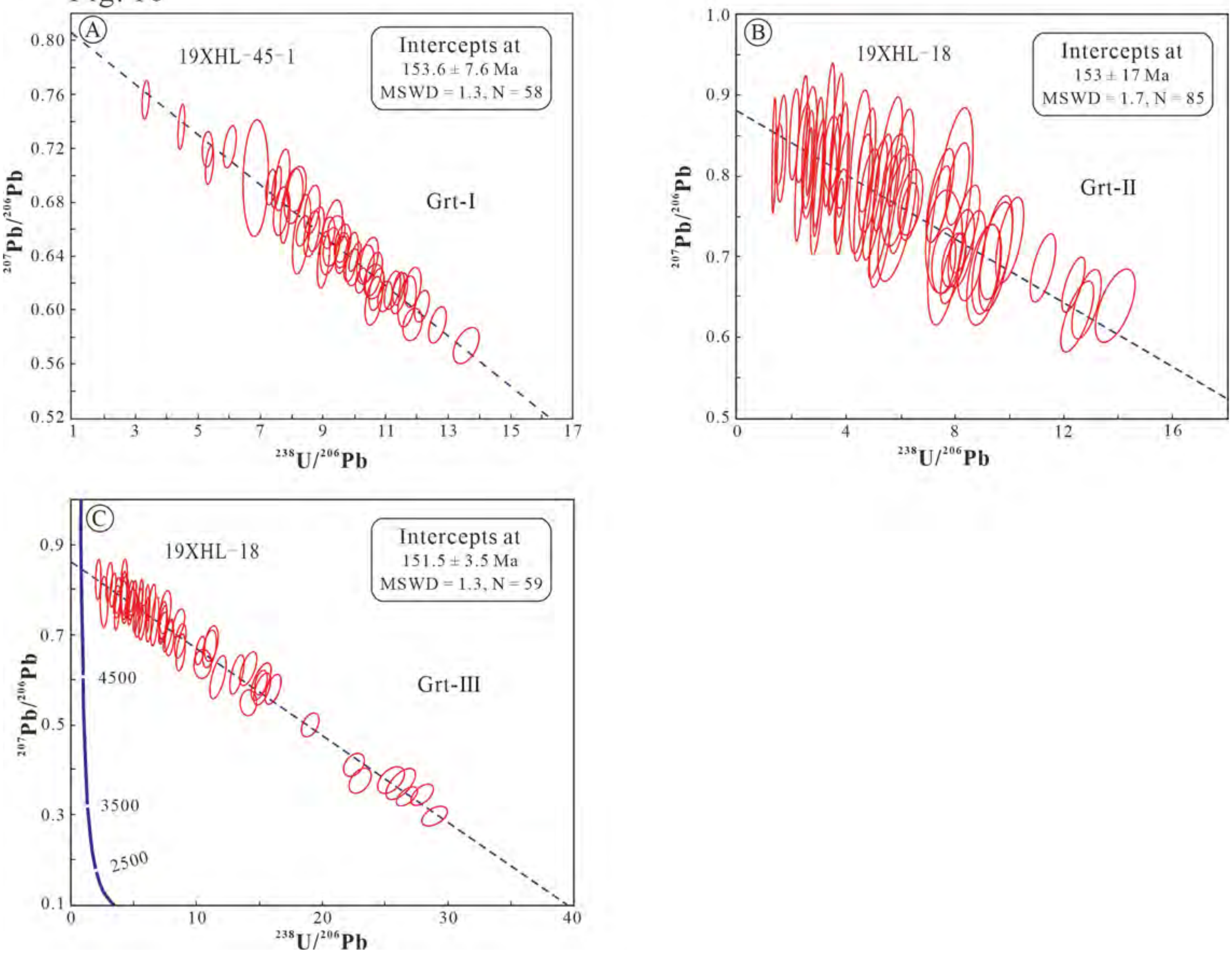
A
19XHL-45-1
Intercepts at
153.6 ± 7.6 Ma
MSWD = 1.3, N = 58
Grt-I
$^{207}Pb/^{206}Pb$
$^{238}U/^{206}Pb$
B
19XHL-18
Intercepts at
153 ± 17 Ma
MSWD = 1.7, N = 85
Grt-II
C
19XHL-18
Intercepts at
151.5 ± 3.5 Ma
MSWD = 1.3, N = 59
Grt-III
4500
3500
2500

DOI: https://doi.org/10.2138/am-2022-8412. http://www.minsocam.org/

Fig. 11

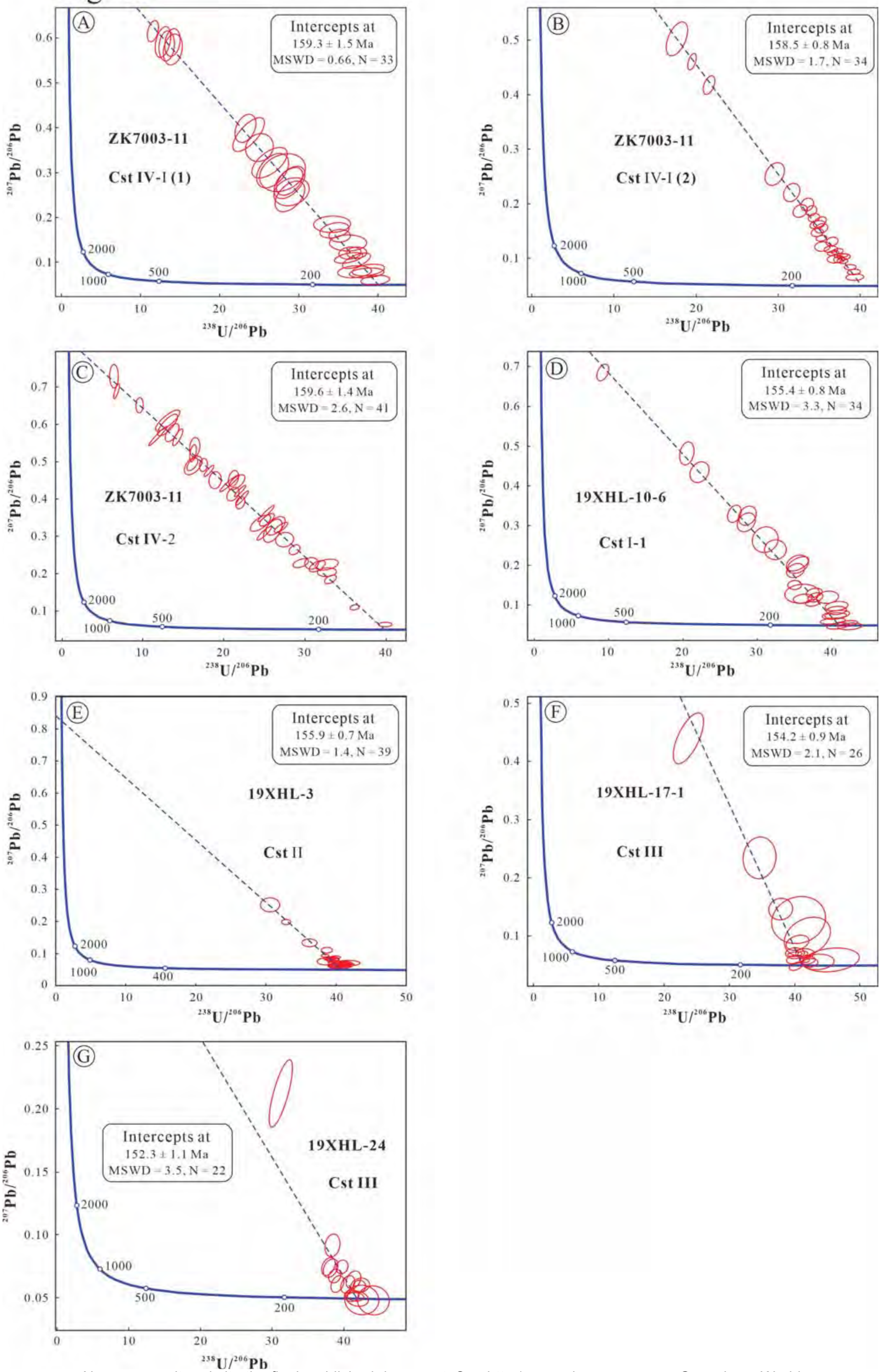

This is the peer-reviewed, final accepted version for American Mineralogist, published by the Mineralogical Society of America.
The published version is subject to change. Cite as Authors (Year) Title. American Mineralogist, in press.
DOI: https://doi.org/10.2138/am-2022-8412. http://www.minsocam.org/

Fig. 12

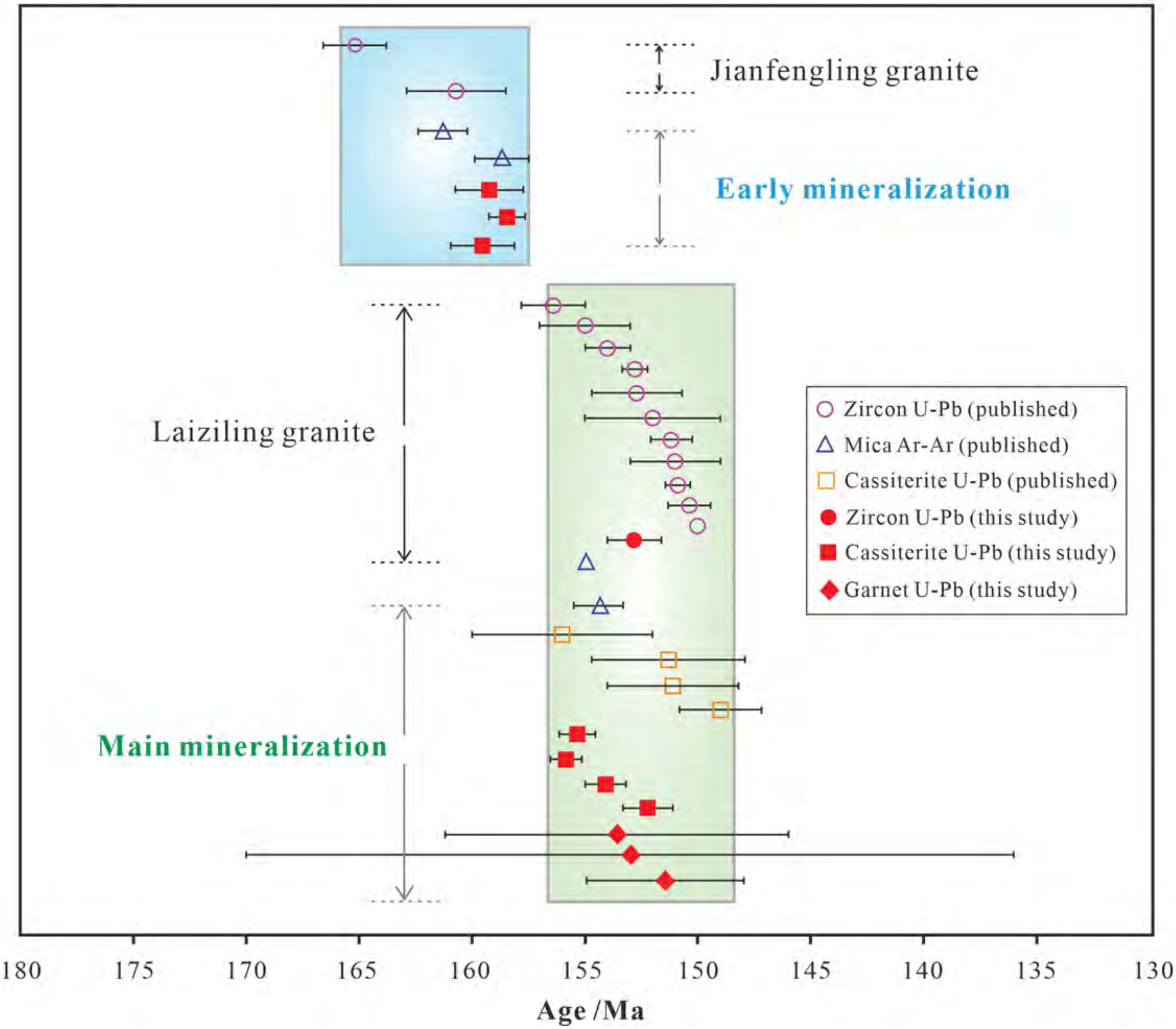

This is the peer-reviewed, final accepted version for American Mineralogist, published by the Mineralogical Society of America.
The published version is subject to change. Cite as Authors (Year) Title. American Mineralogist, in press.
DOI: https://doi.org/10.2138/am-2022-8412. http://www.minsocam.org/

Fig. 13